Research paper

An improved suspension balance model applied to shear-induced phase segregation

Lauren Schlatter [ID], Gabriel Gonçalves da Silva Ferreira [ID], Paulo Laranjeira da Cunha Lage [ID] *

Programa de Engenharia Química/COPPE, Universidade Federal do Rio de Janeiro, PO Box 68502, Rio de Janeiro, RJ, 21941-972, Brazil

ARTICLE INFO

ABSTRACT

When suspensions are subject to non-homogeneous shear, particles migrate towards lower-shear rate regions of the flow due to the anisotropy on the particle phase's normal stress. This phenomenon leads to phase segregation, complicating the interpretation of rheological experimental data for characterising those suspensions. This work presents an improved version of the well-known Suspension Balance Model (SBM), featuring a frame-independent formulation of the particles' normal stress with an improved momentum interpolation scheme that prevents numerical oscillations. The particle's stress model also includes a local formulation for the microscopically generated extra stress, ensuring grid convergence. Our model, implemented in OpenFOAM-v7®, successfully simulated various shear-dominated flows. The simulated Couette rheometric data showed that the characterisation of suspensions from such data could not capture their non-Newtonian behaviour. Besides, the obtained rheological model for the suspensions depended on the geometry of the rheometer, being unable to predict the flow of the same suspension in different conditions and geometries.

1. Introduction

Suspension flows are present in various natural and industrial processes, as in the pharmaceutical, cosmetic, construction, and food industries (Schroën et al., 2017; Drijer et al., 2018; Guazzelli and Pouliquen, 2018). In the oil and gas industry, hydraulic fracturing uses suspensions of solid proppants in the fracking fluid to prevent the fractures' closing after depressurisation of the well (Dontsov and Peirce, 2014). Hydrodynamic effects may dominate suspension flows, characterising the Stokesian regime with negligible Brownian and colloidal effects. In this specific regime, shear-induced migration and phase segregation occur if the flow is subject to non-homogeneous shear, and the non-homogeneous field of particles' concentration results in an apparent viscosity field.

Suspension rheology studies date back to Einstein (1906), who observed that the viscosity of dilute suspensions depended on the particles' volumetric phase fraction. In the following years, many authors attempted to measure the viscosity of suspensions and extrapolate the work of Einstein (1906) to more concentrated suspensions. However, as pointed out by Gadala-Maria and Acrivos (1980), these studies showed significant scattered results. By performing a series of experiments in a Couette cell with neutrally buoyant suspensions, Gadala-Maria and Acrivos (1980) observed deviations from the expected behaviour of a Newtonian fluid, which increased with the dispersed-phase fraction,

and they assigned this behaviour to a shear-induced anisotropy in the structure of the suspended particles.

Experiments conducted by Leighton and Acrivos (1987) provided new significant insights into the shear-induced migration mechanisms. The authors described the phenomena as diffusive fluxes in the direction normal to the shearing surface towards lower shear-rate regions caused by the irreversible displacement of the particles as they interact, proposing empirical equations for these diffusive fluxes. Phillips et al. (1992) adapted these equations to predict the time evolution of the particles' concentration field. This extended formulation, known as the Diffusive Flux Model (DFM), links the diffusive equation for the evolution of the solid-phase fraction field to the conservation equations of the suspension, modelled as an effective Newtonian fluid with properties depending on the local concentration. However, the DFM of Phillips et al. (1992) assumes that migration occurs in the normal direction to the shearing surface. That is true for some specific applications, such as Stokes flow in concentric Couette rheometers, pipes and channels but not for the eccentric Couette flow and flows in cone-and-plate and torsional parallel-plate rheometers.

Nott and Brady (1994) introduced a new approach called the Suspension Balance Model (SBM). Drawing an analogy with molecular systems, these authors macroscopically describe the particles as a continuous phase since they evolve according to Newton's equations of

---

* Corresponding author.
   E-mail addresses: laurenfernandes@peq.coppe.ufrj.br (L. Schlatter), gferreira@peq.coppe.ufrj.br (Gabriel G.S. Ferreira), paulo@peq.coppe.ufrj.br (Paulo L.C. Lage).

motion just as molecules do and obtain averaged transport equations for the dispersed phase. They define a solid-phase effective stress tensor that accounts for non-Newtonian normal and viscous shear stresses, depending on the solid-phase fraction through a particle viscosity coefficient. Later, Morris and Boulay (1999) addressed an anisotropic formulation of the particles' stress when studying the application of the SBM to curvilinear flows, also providing an empirical description of the functional forms for the dependency of the shear and normal stresses of the suspension on the solid-phase fraction. The resulting model was then used to predict the dispersed-phase fraction for suspension flows in different conditions and presented better predictability than the Diffusive Flux Model of Phillips et al. (1992).

Nevertheless, Morris and Boulay (1999) accounted for the normal stress anisotropy in a way that rendered their model frame-dependent. Miller et al. (2009) formulated a two-dimensional frame-invariant form of the particles' normal stress tensor based on a tension-compression local coordinate system. These authors applied their formulation in simulations of channel flows with sharp-edged contraction and expansion and the flow over a cavity. Dbouk et al. (2013a) used this frame-independent formulation to simulate the resuspension of an initially settled suspension in a 2D Couette cell, considering buoyancy effects. More recently, Badia et al. (2022) developed a model similar to the SBM, with a frame-invariant suspension stress formulation based on the model for second-order fluids, commonly used in polymer rheology. The models of Miller et al. (2009) and Badia et al. (2022) are not only frame-invariant but are also designed to predict the suspension behaviour in non-viscosimetric flows with more complex kinematics. Alternatively, adapting the normal stress formulation of Morris and Boulay (1999) to a two-fluid model, Municchi et al. (2019b) developed a simpler frame-invariant model by replacing the unit vectors originally used to define the anisotropic tensor with unit vectors defined using the calculated velocity field for the particles' phase. They validated their proposed frame-invariant formulation for the resuspension case of an initially settled suspension in a 2D Couette cell and the suspension flow in a 3D symmetric herringbone channel.

Phillips et al. (1992) observed that the DFM did not yield the correct behaviour when the shear rate vanishes, as in the centre of a Poiseuille flow, as the model always predicted a maximum packing concentration. Nott and Brady (1994) highlighted this same limitation regarding the SBM. Even though the *macroscopic* shear rate is zero, in such regions, the finite size of the particles and the fluctuations on the particle-size scale generate motion and, consequently, stress. As the shear rate approaches zero at the centre line of Poiseuille flows, the DFM and the SBM predict that the solid-phase fraction should approach maximum packing with a diverging derivative, exhibiting a nonphysical cusp in the solid-phase fraction profile. Thus, it is necessary to include in the particles' stress tensor a term that accounts for this extra stress. Despite acknowledging this problem, Phillips et al. (1992) did not attempt to develop a solution. Nott and Brady (1994) proposed an isotropic non-local formulation based on the definition of the *suspension temperature*, which represents a scalar measurement of the fluctuations of the particles' mean velocity, generated in regions of high shear rates and diffusing to regions of lower shear rates. Nonetheless, this approach requires additional closing parameters and the solution of an additional transport equation for the suspension temperature.

Shortly after, Mills and Snabre (1995) presented an algebraic formulation considering that the extra stress is transmitted through a network of particles interacting via strong lubrication forces over a correlation distance. Morris and Boulay (1999) also employed an algebraic formulation by spatially averaging the shear rate over a volume element. Miller and Morris (2006) further simplified the formulation of Morris and Boulay (1999), proposing an equation for the associated extra shear rate that gained popularity, being used in many of the most recent suspension rheology studies using the SBM and DFM (Dbouk et al., 2013a; Yadav et al., 2015; Siqueira and de Souza Mendes, 2019; Kang and Mirbod, 2020). In these algebraic formulations, the final stress model is dependent on the geometry of the flow, *e.g.*, the correction term is considered for Poiseuille but not for Couette flows. Including the extra stress prevents the divergence of the dispersed-phase fraction profile, even though this is not always necessary. As the physics behind it is always valid, there is little sense in using this term only for some flow configurations.

Using the formulation of Morris and Boulay (1999), the SBM accurately describes the behaviour of viscosimetric suspension flows, including the flows in cone-and-plate and torsional parallel-plate rheometers, for which the DFM of Phillips et al. (1992) fails. Fang et al. (2002) proposed an anisotropic normal stress formulation similar to the one of Morris and Boulay (1999) and incorporated it into the DFM of Phillips et al. (1992). This modified formulation predicts the correct qualitative behaviour of flows in cone-and-plate and torsional parallel-plate rheometers. However, without an extra stress term in the DFM formulation, it still provided results with a diverging derivative of the concentration profile at the centre of Poiseuille flows. Fang et al. (2002) also incorporated their formulation of the anisotropic normal stresses to the SBM of Nott and Brady (1994), adopting the "suspension temperature" approach to account for the extra stress. These authors extensively discussed and compared the application of the modified DFM and SBM to a series of benchmark viscometric flows, including the steady-state Couette, cone-and-plate, circular and planar Poiseuille flows, and the transient flows in a Couette rheometer, eccentric Couette flow, and piston-driven flow.

For eccentric Couette flows, depending on the eccentricity ratio (the distance between the centres of the cylindrical surfaces normalised by their radii difference), a recirculating flow region arises in the wider portion of the gap (Phan-Thien et al., 1995). Using an adaptation of the DFM of Phillips et al. (1992) for two-dimensional flows, Fang and Phan-Thien (1995) simulated the eccentric Couette flow with an eccentricity of 0.5 but could not obtain steady-state results in the presence of the recirculating flow region due to numerical instabilities within this region. Mirbod (2016) studied the eccentric Couette flow for several eccentricity configurations using an anisotropic SBM formulation without accounting for the extra stress, obtaining stable steady-state results for the same cases simulated by Fang and Phan-Thien (1995). However, for eccentricity ratios above 0.842, the simulations of Mirbod (2016) became unstable. Even though the author did not investigate this issue further, she hypothesised that the instabilities were related to steep gradients on the normal stresses.

Recent studies extended the application of the SBM to more complex cases. Kang and Mirbod (2021, 2023) applied an anisotropic formulation of the SBM with no extra stress to simulate flow instabilities and transitions in Taylor–Couette flows. These are intrinsically 3D flows with complex recirculating patterns for Reynolds numbers above $\mathcal{O}\left(10^2\right)$ (Majji et al., 2018; Ramesh et al., 2019; Ramesh and Alam, 2020). Consequently, Taylor–Couette flows do not occur in the Stokes regime, and the simulation of these cases also requires a frame-invariant formulation of the normal stresses to cope with changes in the flow direction. In the works of Kang and Mirbod (2021, 2023) using the SBM, the formulation adopted for the normal stress anisotropy considers a unidimensional angular velocity despite the changes in the flow direction due to the formation of Taylor instabilities.

Also recently, Lu and Christov (2023) used physically-informed neural networks to estimate the ratio of the DFM parameters using available experimental data for Couette flow (Phillips et al., 1992) and Poiseuille 2D channel flow (Koh et al., 1994) of non-Brownian suspensions. Their estimate agreed with Phillips et al. (1992) results for the Couette flow but differed from those for the Poiseuille 2D channel flow, which also vary with the bulk particles' volume fraction. Therefore, they showed that the DFM needs parameters fitting for each flow configuration, which stresses the importance of a model for suspension flow that does not depend on the flow configuration.

Alternatively to the diffusive flux and suspension balance models for dense suspension flows, Boyer et al. (2011) introduced a frictional

approach derived from the theory of dry granular flows. These authors adapted the existing models for dry granular systems to model the stresses in a monodisperse suspension with a jamming limit, *i.e.*, maximum packing fraction, inferior to the random close packing (RCP) limit. Lecampion and Garagash (2014) later extended this formulation to allow for compaction of the particles beyond the jamming limit up to the RCP threshold. Through MRI measurements of concentrated suspension flows in a circular cross-section pipe, Oh et al. (2015) showed that the particles compact and achieve the random close packing limit, forming a solid-like plug at the centre of the pipe. The authors adapt the frictional model as presented by Lecampion and Garagash (2014) to account for the so far neglected normal stress anisotropy, comparing their experimental data to the predictions of this adapted formulation and the original isotropic formulation of Lecampion and Garagash (2014).

All approaches presented so far treat the suspension as an effective fluid, an approximation that only holds for systems with small slip velocities. The study of shear-induced migration is also interesting for multiphase fluid dynamics, where fluid and particles are two interpenetrating phases with their transport equations. Consequently, there is no need to limit the application of the model to systems of rapid relaxation. Using a rather similar approach to the Diffusive Flux Model in the multiphase framework, Tiwari et al. (2009) and Drijer et al. (2018) introduced the effects of shear-induced particle migration in the momentum conservation equations of both fluid and solid phases as a driving force and applied the proposed models to study suspension flow in membrane tubes used for nano- and micro-filtration processes. Also adapting a mixture model to the two-fluid model framework, the frictional rheology model of Boyer et al. (2011) was used by Dontsov and Peirce (2014) to predict the steady flow of a slurry in a rock fracture, considering buoyancy effects. These authors modified the particle-phase stress to include the anisotropic normal stress terms from the formulation of Morris and Boulay (1999). Inkson et al. (2017) used a similar strategy, modifying the general Eulerian model for two-phase flows to include the suspension stress model of Morris and Boulay (1999) and simulating the suspension flow in a 2D Couette cell, a 3D circular cross-section pipe, and an asymmetric channel bifurcation. In their final model, however, the anisotropy of the normal stresses is disregarded. Municchi et al. (2019b) also developed a modified Eulerian model by replacing the stress tensor of the dispersed phase with the particles' stress tensor of Morris and Boulay (1999), accounting for the anisotropy of the normal stresses in a frame-invariant formulation.

This work aimed to improve the current formulation of the SBM focusing on shear-dominated flows of dense, non-Brownian suspensions of monodispersed spherical particles on a Newtonian fluid of matching density. The improved model was implemented in OpenFOAM, assuming the suspension flow in the Stokes regime, creating a robust computational tool that provides the simulation's results at a reasonably low computational cost. The resulting solver was used to validate the improved model against experimental results found in the literature and applied to study the impacts of shear-induced migration on determining the apparent viscosity of suspensions.

The SBM improvements include a new local extra stress model and a correction of the normal stresses in regions with near-uniform velocity. The SBM implementation improvements are a frame-invariant formulation of the normal stresses, an enhanced momentum interpolation scheme, and the correction needed to simulate open conduits using cyclic domains.

We organised this text as follows. Section 2 describes the SBM equations, including our proposed modifications. We proposed a new local extra stress model in Section 2.2.1 and a frame-invariant anisotropic stress tensor model in Section 2.2.3. Section 3 describes the numerical procedure, presenting an improved momentum interpolation procedure in Section 3.1, and a procedure for the simulations of suspension flows in open conduits using cyclic domains in Section 3.3. Section 4 presents the simulated cases and the discussion of their results is presented in Section 5. Section 6 presents our conclusions.

2. Methodology

The suspension balance model is valid for suspension flows with a fast relaxation of the particles' velocities, which allows its representation as a single effective fluid. The particles' Stokes number represents the ratio of the characteristic time of the motion of a suspended particle to the characteristic time of the suspension flow, and it must be small for holding the single effective fluid approximation (Coussot and Ancey, 1999):

$$St = \frac{\rho_p a^2 \dot{\gamma}}{3\pi\mu_f} \ll 1, \tag{1}$$

where ρ_p is the particles' density, a is the particle radius, $\dot{\gamma}$ is the shear rate, and μ_f is the viscosity of the liquid forming the continuous-phase. The subscripts p, f, and s denote averaged properties for the particles' phase, fluid or suspension, respectively. The SBM also assumes the particle–fluid drag force in the Stokes regime, where there is negligible inertia, which is satisfied if the particle's Reynolds number is much smaller than one (Nott and Brady, 1994):

$$Re_p = \frac{\rho_f a^2 \dot{\gamma}}{\mu_f} \ll 1. \tag{2}$$

where ρ_f is the density of the continuous phase.

Moreover, for non-Brownian suspension flow, the Péclet number, which represents the ratio of viscous to Brownian forces, should be large (Coussot and Ancey, 1999):

$$Pe = \frac{6\pi\mu_f \dot{\gamma} a^3}{k_B T} \gg 1, \tag{3}$$

where T is the temperature and k_B is the Boltzmann constant.

2.1. Conservation equations

For an incompressible suspension of neutrally buoyant particles, the resulting particle-phase mass conservation equation is

$$\frac{\partial \phi}{\partial t} + \mathbf{u}_s \cdot \nabla\phi = -\nabla \cdot \mathbf{J}, \tag{4}$$

where ϕ is the dispersed-phase fraction and $\mathbf{u}_s$ is the suspension velocity. The particles' migration flux is defined as $\mathbf{J} = \phi\left(\mathbf{u}_p - \mathbf{u}_s\right)$. For $St \ll 1$, the particles' momentum equation, considering only the drag force between the phases, gives the following expression for $\mathbf{J}$:

$$\mathbf{J} = \frac{2a^2 f(\phi)}{9\mu_f}\nabla \cdot \mathbf{S}_p, \qquad f(\phi) = \left(1 - \frac{\phi}{\phi_m}\right)(1-\phi)^{\alpha-1}, \tag{5}$$

in which $\mathbf{S}_p$ is the particles' phase stress tensor and $f(\phi)$ is the hindrance function, modelled as given by Miller and Morris (2006) with $\alpha = 4$, in which ϕ_m represents the maximum packing fraction.

To obtain a fast computational simulation tool, we restrict the present implementation of the SBM to flows in the Stokes regime. Therefore, by averaging the transport equations over the volume of the suspension, one can obtain its mass and momentum conservation equations:

$$\nabla \cdot \mathbf{u}_s = 0, \tag{6}$$

$$\nabla \cdot \mathbf{S}_s = 0. \tag{7}$$

Eqs. (4), (6) and (7) constitute the set of the SBM transport equations that are solved for the dispersed-phase fraction, the pressure, and the suspension's velocity, respectively.

2.2. Stress tensor models

The stress tensor of the suspension is given by the sum of the particle- and fluid-phase stress tensors:

$$\mathbf{S}_s = \mathbf{S}_p + \mathbf{S}_f. \tag{8}$$

For a Newtonian incompressible fluid as the continuous phase, we have:

$$\mathbf{S}_f = -p\mathbf{I} + 2\mu_f\mathbf{E}, \tag{9}$$

where p is the pressure and the rate of strain tensor is $\mathbf{E} = \frac{1}{2}\left[\nabla\mathbf{u}_s + (\nabla\mathbf{u}_s)^T\right]$.

Morris and Boulay (1999) modelled the particles' stress tensor considering both shear and normal contributions:

$$\mathbf{S}_p = 2\mu_p\mathbf{E} + \mathbf{S}_p^n. \tag{10}$$

They modelled the normal stress tensor as:

$$\mathbf{S}_p^n = -\mu_n\dot{\gamma}\mathbf{Q}, \tag{11}$$

in which the shear rate is calculated by $\dot{\gamma} = \sqrt{2\mathbf{E}:\mathbf{E}}$ and $\mathbf{Q}$ is the anisotropic stress tensor defined by Morris and Boulay (1999):

$$\mathbf{Q} = \sum_{i=1}^{3} \lambda_i\hat{\mathbf{e}}_i\hat{\mathbf{e}}_i, \tag{12}$$

where the unit vectors $\hat{\mathbf{e}}_1$, $\hat{\mathbf{e}}_2$ and $\hat{\mathbf{e}}_3$ represent the directions of the flow velocity, its gradient and vorticity, respectively.

Morris and Boulay (1999) assumed uniform values for λ_i, $i = 1$, 2 and 3, given by $\lambda_1 = 1.0$, $\lambda_2 = 0.8$ and $\lambda_3 = 0.5$, which ensures the anisotropic behaviour and gives qualitative agreement with experimental data and Stokesian dynamics simulations results. We adopted those constant values, except for the modification proposed to λ_3 in regions of near-constant velocity, discussed in Section 2.2.3.

For some flow configurations, it is possible to choose a coordinate system whose versors' directions coincide with those of $\hat{\mathbf{e}}_1$, $\hat{\mathbf{e}}_2$ and $\hat{\mathbf{e}}_3$, resulting in a frame-dependent formulation in which tensor $\mathbf{Q}$ is uniform.

The viscosities μ_p and μ_n are known as the particle shear and normal viscosities and depend on the dispersed-phase fraction. We followed the rheological model of Morris and Boulay (1999), which gives:

$$\frac{\mu_p}{\mu_f} = 2.5\phi\left(1 - \frac{\phi}{\phi_m}\right)^{-1} + K_s\left(1 - \frac{\phi_m}{\phi}\right)^{-2} \tag{13}$$

and

$$\frac{\mu_n}{\mu_f} = K_n\left(1 - \frac{\phi_m}{\phi}\right)^{-2}, \tag{14}$$

with $K_s = 0.1$ and $K_n = 0.75$. Notice that Eq. (13) corrects a typographical error in the equation given by Morris and Boulay (1999). The viscosity of the suspension is the sum of the shear viscosities of both phases:

$$\frac{\mu_s}{\mu_f} = \frac{\mu_p}{\mu_f} + 1 = 2.5\phi\left(1 - \frac{\phi}{\phi_m}\right)^{-1} + K_s\left(1 - \frac{\phi_m}{\phi}\right)^{-2} + 1. \tag{15}$$

2.2.1. Extra stress contribution

To model the extra stress that is generated at the particle-size scale and transmitted by lubrication forces throughout the particles' assemblage, Miller and Morris (2006) added a constant value to the calculated shear rate in Eq. (11), rewriting the particles' normal stress as

$$\mathbf{S}_p^n = -\mu_n\left(\dot{\gamma} + \dot{\gamma}_{nl}\right)\mathbf{Q}, \tag{16}$$

and defining the non-local shear rate, $\dot{\gamma}_{nl}$, using a dimensionally sound relation using the particle size, a, the characteristic length of the macroscopic flow, L_c, and the maximum velocity magnitude of the suspension, u_{max}, given by:

$$\dot{\gamma}_{nl} = f(\epsilon)\frac{u_{max}}{L_c}, \qquad \epsilon = \frac{a}{L_c}, \tag{17}$$

assuming $f(\epsilon) = \epsilon$ for pipe or channel flows and $f(\epsilon) = 0$ otherwise.

As mentioned in Section 1, adding the extra shear rate term to avoid the divergence of the predicted dispersed-phase fraction gradient is only necessary for flows with a null shear rate region within the domain. However, the physics of the stress transmission in concentrated suspensions responsible for generating the extra stress is always

present, so there is little sense in adding the correction term for some flow configurations and not others.

Our proposed model defines the particles' normal stress tensor by:

$$\mathbf{S}_p^n = -\mu_n\dot{\gamma}\mathbf{Q} + \mathbf{S}_p^e, \qquad \mathbf{S}_p^e = -\mu_n\dot{\gamma}_e\mathbf{I}, \tag{18}$$

with $\mathbf{S}_p^e$ representing the extra stress tensor and $\dot{\gamma}_e$ the associated extra shear rate.

Since the extra stress represents the momentum transport at the particle-size scale associated with the particles' velocity fluctuations, we modelled the extra shear rate as the magnitude of these velocity fluctuations between neighbouring particles divided by their clearance, c. We assumed the particles' velocity fluctuations to be proportional to the *local* suspension velocity magnitude, yielding:

$$\dot{\gamma}_e = \frac{k}{c}\sqrt{\mathbf{u}_s \cdot \mathbf{u}_s}, \tag{19}$$

where we adopted $c = 2a$ because the clearance between neighbouring particles in a dense suspension is of the same order of magnitude as their diameter, and the fitting parameter k is an adjusted factor that should be much smaller than one. It should be large enough to prevent the divergence of the gradient of the dispersed-phase fraction where $\dot{\gamma} = 0$ but small enough to be negligible in the flow regions with large shear rates.

2.2.2. Effect of the extra stress contribution

To compare the different formulations for the particles' normal stress tensor, consider the steady-state and fully developed suspension flow in a circular cross-section pipe, with $\hat{\mathbf{e}}_1 = \hat{\mathbf{e}}_z$ and $\hat{\mathbf{e}}_2 = \hat{\mathbf{e}}_r$ in cylindrical coordinates. In these conditions, $\mathbf{u}_s = u_s(r)\hat{\mathbf{e}}_z$, there is no z dependence, and the particles' migration flux is null.

According to Eq. (5), the radial component of the particles' migration flux, which must be zero, is given by:

$$J_r = \frac{2a^2 f(\phi)}{9\mu_f}\left[\frac{1}{r}\frac{d\left(rS_{p_{rr}}\right)}{dr} - \frac{S_{p_{\theta\theta}}}{r}\right] = 0. \tag{20}$$

Since $f(\phi) \neq 0$, $\forall\phi$, the terms within the square brackets must be zero.

For the particles' normal stress tensor model given by Eq. (11), one can obtain the following expression for the derivative of the concentration profile:

$$\frac{d\phi}{dr} = \left[\frac{\lambda_3 - \lambda_2}{\lambda_2 r} - \frac{1}{\dot{\gamma}}\frac{d\dot{\gamma}}{dr}\right]\left(\frac{1}{\mu_n}\frac{d\mu_n}{d\phi}\right)^{-1}, \tag{21}$$

which must be null at $r = 0$ due to the axial symmetry. However, for an arbitrary model for $\mu_n(\phi)$, Eq. (21) cannot represent the correct behaviour of $d\phi/dr$ at $r = 0$ as both terms within the square brackets go to infinity at this point. The term $(1/\dot{\gamma})d\dot{\gamma}/dr$ goes to infinity at $r = 0$ because $\dot{\gamma} = |du_s/dr|$ is an even function of r with a null value at this point. Using the assumption of different uniform values for λ_2 and λ_3, the term $(\lambda_3 - \lambda_2)/r$ also goes to infinity at $r = 0$.

The singularity of the first term within the square brackets of Eq. (21) disappears if $\lambda_2 = \lambda_3$ within a region that includes $r = 0$, and the next section discusses this issue. The extra stress models should remove the singularity of the second term, eliminating the non-physical cusp of the ϕ profile at the centre-line of the pipe.

Repeating the derivation of the radial derivative of the dispersed-phase fraction using the non-local model of Miller and Morris (2006) for the extra stress contribution (Eq. (16)), one obtains

$$\frac{d\phi}{dr} = \left[\frac{\lambda_3 - \lambda_2}{\lambda_2 r} - \frac{1}{\left(\dot{\gamma} + \dot{\gamma}_{nl}\right)}\frac{d\dot{\gamma}}{dr}\right]\left(\frac{1}{\mu_n}\frac{d\mu_n}{d\phi}\right)^{-1}, \tag{22}$$

since $d\dot{\gamma}_{nl}/dr = 0$.

The same derivation using our proposed formulation given by Eq. (18) gives:

$$\frac{d\phi}{dr} = \frac{1}{\left(\lambda_2\dot{\gamma} + \dot{\gamma}_e\right)}\left[\frac{\dot{\gamma}\left(\lambda_3 - \lambda_2\right)}{r} - \frac{d\left(\lambda_2\dot{\gamma} + \dot{\gamma}_e\right)}{dr}\right]\left(\frac{1}{\mu_n}\frac{d\mu_n}{d\phi}\right)^{-1}, \tag{23}$$

where $\dot{\gamma}_e = k u_s^2/(2a)$ and $d\dot{\gamma}_e/dr = k u_s (du_s/dr)/a$.

The second terms within the square brackets in Eqs. (22) and (23) are not singular at $r = 0$, but the first terms are as long as $\lambda_2 \neq \lambda_3$. The model for $\mu_n(\phi)$ can mitigate this singularity. Specifically, when using the particles' normal viscosity model from Eq. (14), $(d\mu_n/d\phi)/\mu_n$ goes to $-\infty$ as $\phi \to \phi_m$. For dense suspensions, the particles' phase fraction can achieve this limiting value at $r = 0$, leading to $d\phi/dr = 0$ at this point and a smooth ϕ profile.

In contrast to the non-local correction proposed by Miller and Morris (2006), our formulation yields a non-constant profile for $\dot{\gamma}_e$, which presents a minimum value of $\dot{\gamma}_e$ at the pipe (or channel) walls, where its value is negligible when compared to the maximum shear rate achieved at this region, and a maximum value at the centre line, where the shear rate is null, flattening the phase-fraction profile. The main advantage of the proposed extra stress with local extra shear rate, Eqs. (18) and (19), is its general application to any flow configuration.

2.2.3. Frame-invariant formulation of the anisotropic stress tensor

As mentioned, the formulation of Morris and Boulay (1999) for the anisotropic stress tensor $\mathbf{Q}$ is frame-dependent and restricted to a few flow configurations. In a two-fluid model framework, Municchi et al. (2019b) presented a frame-invariant formulation based on the local calculation of the unit vectors defining $\mathbf{Q}$ in Eq. (12) from the particles' phase velocity field. For the suspension balance model, we adapted this formulation by defining these unit vectors using the suspension velocity field:

$$\hat{\mathbf{e}}_1 = \frac{\mathbf{u}_s}{\|\mathbf{u}_s\|}, \qquad \hat{\mathbf{e}}_3 = \frac{\nabla \times \mathbf{u}_s}{\|\nabla \times \mathbf{u}_s\|}, \qquad \hat{\mathbf{e}}_2 = \hat{\mathbf{e}}_1 \times \hat{\mathbf{e}}_3. \qquad (24)$$

The calculations expressed in Eq. (24) can be challenging in some situations. For the pressure-driven flow in a cylindrical pipe, migration of the particles towards the centre-line of the flow causes a blunting of the velocity profile, creating a plateau, that is, a region where the concentration and velocity fields are uniform. In this region, the calculation of the vorticity and velocity gradient directions are undefined, making it impossible to determine the unit vectors $\hat{\mathbf{e}}_2$ and $\hat{\mathbf{e}}_3$ using Eq. (24).

However, any two orthogonal unit vectors on the velocity plateau's plane are suitable for defining the local coordinate system because, in this situation, there is no longer a physical difference between directions $\hat{\mathbf{e}}_2$ and $\hat{\mathbf{e}}_3$. Therefore, their respective coefficients λ_2 and λ_3 should be equal in a plateau region.

When using the local coordinate system from Eq. (24) in a region where the velocity field is uniform or near uniform, this problem presents itself as a numerical issue due to the difficulty of accurately calculating $\hat{\mathbf{e}}_3$. However, it also represents a modelling misconception of the anisotropic stress tensor when its definition, given by Eq. (12), assumes $\lambda_2 \neq \lambda_3$ for all flow domain as proposed by Morris and Boulay (1999). As shown by Eq. (23), λ_2 and λ_3 must be equal within a velocity plateau region to avoid a singularity in the derivative of the particles' concentration.

Understanding the implications of altering the definitions of unit vectors and their coefficients, we refer to Eq. (23) for the derivative of the particles' phase fraction profile for the steady-state and fully developed suspension flow in a circular cross-section pipe, using our proposed model for the extra stress. This equation reveals that any discontinuity in either λ_2 or λ_3 results in a $d\phi/dr$ discontinuity. Given our conclusion that λ_2 and λ_3 must be equal in regions with $d\phi/dr = 0$, it is crucial to avoid such discontinuities. To achieve this, we have opted to maintain λ_2 constant across the entire domain so we would not disturb the two terms in Eq. (23) that depend on λ_2 only. Since both coefficients should be equal inside the plateau region, we defined a transition for λ_3 from its original value of 0.5 in the outer region of the plateau to a value equal to λ_2 (0.8) inside the plateau. We employed a logistic function to ensure the smoothness of the transition, avoiding the discontinuities mentioned above in $d\phi/dr$.

A non-constant formulation for the coefficients λ_i, $i = 1$, 2 and 3 in Eq. (12) was studied experimentally by Dbouk et al. (2013b)

by performing a series of experiments for the torsional suspension flow between parallel discs. However, in their proposed model, the coefficients are written as a function of the particles' phase fraction, and the results show a larger difference between λ_2 and λ_3 as the dispersed-phase fraction approaches the maximum packing. According to the above analysis, this is the opposite of the physically expected behaviour of a near-jammed suspension.

3. Numerical procedure

The set of coupled non-linear partial differential equations presented in the previous section was implemented and solved using OpenFOAM-v7® , an open-source CFD package written in C++ that uses the finite volume method to solve field equations (Weller et al., 1998). Since we assumed the suspension incompressible, the formulation in this section uses the modified pressure, $p^* = p/\rho$, and the kinematic viscosity, $\nu = \mu/\rho$.

The standard pressure–velocity coupling algorithm in OpenFOAM uses the Rhie and Chow (1983) interpolation method (see Supplementary Material). This coupling algorithm may present difficulties when high gradients exist in the force terms of the momentum equation (Passalacqua and Fox, 2011). The introduction of the normal stress of the particulate phase, $\nabla \cdot \mathbf{S}_p^n$, similarly to a pressure gradient term, with a non-uniform formulation for the anisotropic stress tensor $\mathbf{Q}$ enhances these problems, generating oscillations in the solid-phase fraction profile. To remedy this, we followed the procedure described by Municchi et al. (2019b), splitting the normal stress terms into contributions from the spatial variations of the normal viscosity and the shear rate. The resulting improved momentum interpolation scheme is presented in the following subsection.

3.1. Improved momentum interpolation

Considering the suspension stress given by Eqs. (8), (9), and (10), one can write the momentum conservation equation for the suspension (Eq. (7)) as

$$-\nabla^2 (\nu_s \mathbf{u}_s) - \nabla \cdot \left[\nu_s (\nabla \mathbf{u}_s)^T \right] + \nabla \cdot \mathbf{S}_p^n = -\nabla p^*. \qquad (25)$$

Using the particles' phase normal stress tensor with our extra stress contribution given in Eq. (18), and splitting $\nabla \cdot \mathbf{S}_p^n$, Eq. (25) can be rewritten as

$$-\nabla^2 (\nu_s \mathbf{u}_s) - \nabla \cdot \left[\nu_s (\nabla \mathbf{u}_s)^T \right] + \nu_n \left[\nabla \cdot (\dot{\gamma} \mathbf{Q}) + \nabla \dot{\gamma}_e \right] =$$
$$-\nabla p^* - \dot{\gamma} \frac{d\nu_n}{d\phi} \nabla \phi \cdot \mathbf{Q} - \dot{\gamma}_e \frac{d\nu_n}{d\phi} \nabla \phi. \qquad (26)$$

Following the finite volume discretisation procedure as described in Jasak (1996), partial discretisation of Eq. (26) results in the linear system $\mathcal{M} \mathbf{u}_s = \mathcal{B} - \nabla p^*$, in which $\mathcal{B}$ is the vector of source terms and $\mathcal{M}$ is the coefficient matrix. With an implicit discretisation of the Laplacian term in Eq. (26), discretisation of its left-hand side leads to the momentum predictor equation:

$$\mathcal{A} \mathbf{u}_s - \mathcal{H} = -\nabla p^* - \dot{\gamma} \frac{d\nu_n}{d\phi} \nabla \phi \cdot \mathbf{Q} - \dot{\gamma}_e \frac{d\nu_n}{d\phi} \nabla \phi, \qquad (27)$$

where $\mathcal{A}$ is the diagonal part of $\mathcal{M}$ and vector $\mathcal{H}$ is defined by $\mathcal{H} = (\mathcal{A} - \mathcal{M})\mathbf{u}_s + \mathcal{B}$. The momentum predictor equation is solved for the velocity $\mathbf{u}_s$ using the pressure field from the previous iteration.

From Eq. (27), using the notation $1/\mathcal{A} \equiv \mathcal{A}^{-1}$, we obtain the momentum correction equation:

$$\mathbf{u}_s = \frac{\mathcal{H}}{\mathcal{A}} - \frac{1}{\mathcal{A}} \left[\nabla p^* + \dot{\gamma} \frac{d\nu_n}{d\phi} \nabla \phi \cdot \mathbf{Q} + \dot{\gamma}_e \frac{d\nu_n}{d\phi} \nabla \phi \right], \qquad (28)$$

in which the terms inside the square brackets on the right-hand side are evaluated explicitly using the updated pressure field.

To obtain the pressure equation, the volumetric fluxes are calculated from

$$\varphi = (\mathbf{u}_s)_{cf} \cdot \mathbf{A} + \varphi_\Sigma + \left[\left(\frac{\nabla p^*}{\mathcal{A}} \right)_{cf} - \left(\frac{1}{\mathcal{A}} \right)_{cf} \nabla_{cf} p^* \right] \cdot \mathbf{A}, \qquad (29)$$

in which $\mathbf{A} = A\hat{\mathbf{n}}$ is a vector with magnitude equal to the cell's face area, A, in the direction of its normal unit vector $\hat{\mathbf{n}}$, and the operator $\nabla_{cf} p^*$ represents the pressure gradient at the cell face calculated using the cell-centred values of the pressure at the neighbour control volumes. For other occurrences, the subscript cf indicates the interpolation from the cell-centred values to the cell faces. The stress tensor correction, φ_Σ, is given as

$$\varphi_\Sigma = \left[\left(\frac{\dot{\gamma}}{\mathcal{A}} \frac{dv_n}{d\phi} \nabla\phi \cdot \mathbf{Q} + \frac{\dot{\gamma}_e}{\mathcal{A}} \frac{dv_n}{d\phi} \nabla\phi \right)_{cf} \right. $$
$$\left. - \left(\frac{1}{\mathcal{A}} \right)_{cf} \left(\dot{\gamma} \frac{dv_n}{d\phi} \right)_{cf} \nabla_{cf}\phi \cdot (\mathbf{Q})_{cf} - \left(\frac{1}{\mathcal{A}} \right)_{cf} \left(\dot{\gamma}_e \frac{dv_n}{d\phi} \right)_{cf} \nabla_{cf}\phi \right] \cdot \mathbf{A}. \tag{30}$$

Then, replacing $\mathbf{u}_s$ from Eq. (28) into Eq. (29), the final expression for the volumetric flux of the suspension at the cell faces is

$$\varphi = \left[\left(\frac{\mathcal{H}}{\mathcal{A}} \right)_{cf} - \frac{\nabla_{cf} p^*}{\mathcal{A}_{cf}} - \left(\frac{1}{\mathcal{A}} \right)_{cf} \left(\dot{\gamma} \frac{dv_n}{d\phi} \right)_{cf} \nabla_{cf}\phi \cdot (\mathbf{Q})_{cf} \right. $$
$$\left. - \left(\frac{1}{\mathcal{A}} \right)_{cf} \left(\dot{\gamma}_e \frac{dv_n}{d\phi} \right)_{cf} \nabla_{cf}\phi \right] \cdot \mathbf{A}. \tag{31}$$

Combining the mass conservation equation for the suspension, Eq. (6), with Eq. (31), we find

$$\nabla_D \cdot \left[\left(\frac{\mathcal{H}}{\mathcal{A}} \right)_{cf} \cdot \mathbf{A} - \left(\frac{1}{\mathcal{A}} \right)_{cf} \left(\dot{\gamma} \frac{dv_n}{d\phi} \right)_{cf} \nabla_{cf}\phi \cdot (\mathbf{Q})_{cf} \cdot \mathbf{A} \right. $$
$$\left. - \left(\frac{1}{\mathcal{A}} \right)_{cf} \left(\dot{\gamma}_e \frac{dv_n}{d\phi} \right)_{cf} \nabla_{cf}\phi \cdot \mathbf{A} \right] = \nabla_D \cdot \left[\left(\frac{1}{\mathcal{A}} \right)_{cf} \nabla_{cf} p^* \cdot \mathbf{A} \right], \tag{32}$$

where the operator $\nabla_D(\cdot)$ represents the numerical discretisation of the divergent operator using the finite volume method. Eq. (32) is solved for the pressure field, with the implicit discretisation of the Laplacian of the pressure on the right-hand side and explicit evaluation of the remaining terms.

Applying the finite volume discretisation procedure to the mass conservation equation of the particulate phase (Eq. (4)) for an incompressible suspension yields

$$V \frac{\phi - \phi^o}{\Delta t} + \nabla_D \cdot (\phi_{cf} \varphi) = -\nabla_D \cdot (\mathbf{J}_{cf} \cdot \mathbf{A}), \tag{33}$$

in which V is the cell volume, Δt is the time step, the superscript o indicates the previous time instant, and the time operator was evaluated by the implicit Euler method. In Eq. (33) the divergence operator in the left-hand side is evaluated implicitly and the one on the right-hand side explicitly.

3.2. Implementation of the anisotropic stress tensor

In our formulation of the anisotropic tensor $\mathbf{Q}$, we identify the presence of a flow region with an almost uniform velocity field by evaluating the normalised magnitude of the velocity's gradient:

$$\kappa = \frac{\|\nabla \mathbf{u}_s\|}{\max(\|\nabla \mathbf{u}_s\|)}. \tag{34}$$

If κ is larger than the stipulated tolerance τ, the unit vectors are defined as described in Eq. (24). Otherwise, $\hat{\mathbf{e}}_1$ and $\hat{\mathbf{e}}_2$ are calculated using this equation but with a redefined $\hat{\mathbf{e}}_3$.

To redefine $\hat{\mathbf{e}}_3$, we take the vector product of $\hat{\mathbf{e}}_1$ with the three unit vectors of the Cartesian coordinate system, $\hat{\mathbf{e}}_i^{(c)}$, and calculate their magnitudes, whose largest possible value is one, which occurs when they are orthogonal. Thus, we choose the Cartesian unit vector $\hat{\mathbf{e}}_j^{(c)}$ that gives the largest value of $\|\hat{\mathbf{e}}_1 \times \hat{\mathbf{e}}_j^{(c)}\|$, and define $\hat{\mathbf{e}}_3 = \hat{\mathbf{e}}_1 \times \hat{\mathbf{e}}_j^{(c)} / \|\hat{\mathbf{e}}_1 \times \hat{\mathbf{e}}_j^{(c)}\|$. Therefore, the new definition of the local coordinate system throughout

the whole domain is

$$\hat{\mathbf{e}}_1 = \frac{\mathbf{u}_s}{\|\mathbf{u}_s\|}, \qquad \hat{\mathbf{e}}_3 = \begin{cases} \dfrac{\nabla \times \mathbf{u}_s}{\|\nabla \times \mathbf{u}_s\|}, & \kappa \geq \tau \\ \dfrac{\hat{\mathbf{e}}_1 \times \hat{\mathbf{e}}_j^{(c)}}{\|\hat{\mathbf{e}}_1 \times \hat{\mathbf{e}}_j^{(c)}\|}, & \kappa < \tau \end{cases}, \qquad \hat{\mathbf{e}}_2 = \hat{\mathbf{e}}_1 \times \hat{\mathbf{e}}_3. \tag{35}$$

For cases with plane symmetry, our numerical code identifies the direction with the *empty* boundary conditions in OpenFOAM and verifies if $\hat{\mathbf{e}}_3$ has this direction. If this happens, $\hat{\mathbf{e}}_1$ and $\hat{\mathbf{e}}_2$ are calculated from:

$$\hat{\mathbf{e}}_1 = \frac{\mathbf{u}_s}{\|\mathbf{u}_s\|}, \qquad \hat{\mathbf{e}}_2 = \hat{\mathbf{e}}_1 \times \hat{\mathbf{e}}_3. \tag{36}$$

The code also allows the option of making the unit vectors $\hat{\mathbf{e}}_i$ in Eq. (12) equal to the Cartesian unit vectors, $\hat{\mathbf{e}}_i^{(c)}$. Even though our local coordinate system is left-handed due to the definition of $\hat{\mathbf{e}}_2$, the usage of the right-handed Cartesian system does not affect the calculation of $\mathbf{Q}$ because it is a diagonal tensor in the local coordinate system.

As discussed in Section 2.2.3, when $\kappa < \tau$, the coefficient λ_3 in Eq. (12) must tend to the λ_2 value of 0.8. We use a smoothing function $g(h)$ to make the λ_3 value changes from 0.5 for a region where $\kappa \geq \tau$ to 0.8 in the region where $\kappa < \tau$:

$$\lambda_3 = 0.3g(h) + 0.5. \tag{37}$$

The smoothing function was defined as

$$g(h) = \frac{1}{1 + e^{bh}}, \qquad \tanh h = \kappa - \kappa_0. \tag{38}$$

Parameter b in Eq. (38) determines the steepness of the transition and should be positive, so λ_3 decreases as κ increases. The value of κ_0 defines the midpoint of the transition between the two regions with different constant λ_3 values. To guarantee that this transition starts at $\kappa = \tau$, we admit a small error, δ, in $g(h)$ at this position, which allows us to relate the parameters using Eq. (38). Then, κ_0 is calculated by

$$\kappa_0 = \tau - \tanh \hat{h}, \qquad \hat{h} = \frac{1}{b} \ln \left(\frac{\delta}{1 - \delta} \right), \tag{39}$$

and the model parameters to be defined are τ, b and δ. We used $\tau = 0.07$, $b = 150$ and $\delta = 0.1\%$ in all our simulations.

3.3. Fully-developed flow simulations using cyclic domains

A cyclic domain is a convenient geometrical simplification that provides large speedups for simulating the fully developed steady-state velocity and phase fraction profiles for flow in channels and pipes of constant cross-section, A_c. This domain represents a small duct length with just one mesh cell, using periodic boundary conditions in the flow direction. However, these simulations of multiphase flows need corrections for the phase fraction fields, as explained below.

For the simulation of the developing flow in a duct using a lengthy domain, one usually prescribes uniform velocity and phase fraction profiles at the inlet boundary with magnitudes $\bar{u}$ and ϕ_{IN}, respectively. At the steady state, the mass conservation principle states that the flow rate for each phase at any duct cross-section is the same. For the SBM simulations, the suspension and particles' phase flow rates are given by:

$$Q_s = \int_{A_c} \mathbf{u}_s \cdot \hat{\mathbf{n}} \, dA, \qquad Q_p = \int_{A_c} \phi \mathbf{u}_s \cdot \hat{\mathbf{n}} \, dA, \tag{40}$$

where $\hat{\mathbf{n}}$ is a unit vector normal to the cross-section area and oriented in the flow direction. For phases with equal density, the ratio of Q_p/Q_s is the mass-flow average of the particles' phase fraction and must be the same for all cross-sections at the steady state. For a uniform particles' phase fraction at the inlet, conservation of the particle's phase flow rate yields

$$Q_p = \phi_{IN} Q_s = \int_{A_c} \phi \mathbf{u}_s \cdot \hat{\mathbf{n}} \, dA. \tag{41}$$

The simulation in a cyclic domain starts imposing uniform velocity and phase fraction profiles at the inlet boundary. However, the outlet

Table 1

Discretisation schemes used in all performed simulations (entries for the *fvSchemes* dictionary for the OpenFOAM cases).

Term	Method
Gradient (default)	*leastSquares/Gauss linear*
$\nabla \mathbf{u}_s$	*leastSquares*
Surface normal gradient	*corrected*
Laplacian	*Gauss linear corrected*
Divergent (default)	*Gauss linear*
$\nabla \cdot (\phi \mathbf{u}_s)$	*Gauss limitedLinear 1*
Interpolation	*linear*
d/dt	*Euler*

Table 2

Numerical methods used to solve the linear systems, their absolute and relative tolerances (entries for the *fvSolutions* dictionary for the OpenFOAM cases).

	ϕ	p^*	$\mathbf{u}_s$
Linear solver	PBiCG	PCG	PCG
Pre-conditioner	DILU	DIC	DIC
Absolute tolerance	10^{-9}	10^{-10}	10^{-9}
Relative tolerance	0	0.001	0
Final relative tolerance[a]	–	0	–

[a] For the final non-orthogonal correction.

Table 3

Description of the different suspensions considered in our simulations and their properties.

Suspension ID	ϕ_{IN}	ϕ_m	ρ_p (kg/m^3)	ρ_f (kg/m^3)	μ_f (Pa·s)	a (µm)
S1	0.55	0.68	1182	1182	9.45	337.5
S2	0.50	0.68	1190	1190	4.8	50
S3	0.55	0.64	1056	1050	3.6	70
S4	0.35	0.64	1056	1050	3.6	70
S5	0.20	0.64	1056	1050	3.6	70
S6	0.50	0.68	1182	1182	4.95	337.5

fields are continuously mapped to the inlet boundary along the solution iterations. During the simulation, when the fields are not yet converged to the fully developed steady-state flow, there is no guarantee that the mass-flow average of the particles' phase fraction at the outlet cross-section would be equal to the value imposed by the initial conditions. Thus, to accurately use the cyclic domain simplification, our code applies the following correction to the particles' phase fraction field at the end of each time step:

$$\phi^* = \frac{Q_s \, \phi_{IN}}{Q_p} \, \phi, \tag{42}$$

where ϕ^* is the corrected particles' phase fraction field. The reader should note that $\phi_{IN} Q_s / Q_p = 1$ when the solution convergences to the fully developed steady-state flow.

3.4. Solution algorithm

Eqs. (27), (32) and (33) were solved using an adaptation of the SIMPLE coupling algorithm (Patankar and Spalding, 1972). Fig. 1 describes the algorithm, where ϵ represents all the calculated variables. This algorithm also applies to the equivalent equations using OpenFOAM's standard momentum interpolation method. The number of correction steps (*nCorrectors*) and non-orthogonal correction iterations (*nNonOrthCorrs*) were chosen considering the characteristics of each studied case, which are described in Section 4.

Table 1 gives the numerical schemes adopted for OpenFOAM's finite volume discretisation procedure. We chose to use schemes with non-orthogonality corrections for the Laplacian and surface normal gradient operators, which are applied only for simulations using non-orthogonal grids. The *Gauss limitedLinear 1* scheme is a flux-limited blend of the upwind scheme (used in regions with high gradients) and linear schemes, for which the coefficient value equal to 1 implies the strongest limiter action. Depending on their performances, we discretised the gradient terms using either the *Gauss linear* or *leastSquares* methods. The only exception is $\nabla \mathbf{u}_s$, for which *leastSquares* was always employed. Greenshields (2019) gives more information on the discretisation methods.

During the solution of each linear system, the residual is calculated as the normalised absolute difference between the magnitude of the left and right-hand sides of the equation. Then, the linear system is solved iteratively until either this residual falls below the specified tolerance, which is known as the absolute tolerance criteria, or until the ratio between the current and the initial residuals falls below the specified relative tolerance (Greenshields, 2019). Eq. (33) was solved using the preconditioned bi-conjugate gradient method (PBiCG) with diagonal incomplete LU (DILU) factorisation. For the pressure and velocity equations, we used the preconditioned conjugate gradient method (PCG) with diagonal incomplete Cholesky factorisation (DIC), except for simulations with larger meshes (over 50000 grid cells), when we employed the multigrid method using a Gauss–Seidel smoother for the pressure equation solution. Table 2 summarises the linear solvers used for all simulations and their convergence criteria. More information on the linear system's solution methods can be found in Golub and van Loan (2013).

4. Case description

We simulated channel and pipe Poiseuille flows, and concentric and eccentric Couette flows, including conditions for which data were available for validation. Table 3 summarises the properties for all considered suspensions. Fig. 2 depicts the flow configurations, for which we described the details of the validation cases in the following. We assured spatial convergence by performing a grid convergence study for all validation cases. The Supplementary Material gives the details of this procedure.

4.1. Concentric Couette flow

First, we simulated the flow of a suspension of poly-methyl methacrylate (PMMA) particles dispersed in a Newtonian oil (suspension S1) in a concentric wide-gap Couette cell, reproducing the experimental study of Phillips et al. (1992). The simulations start from a homogeneous suspension, and particles migrate as the inner cylinder starts spinning with angular velocity $\omega = 1$ rps. We stopped the simulations once the solid-phase fraction and torque at the inner cylinder reached the steady state. Assuming axisymmetric flow, we performed one-dimensional simulations in a wedge geometry to evaluate the original formulation of the SBM with the frame-dependent anisotropic stress tensor $\mathbf{Q}$. We also carried out 2D simulations using our proposed model with the frame-invariant formulation. Figs. 3(a) and 3(b) show the computational grids for 1D and 2D simulation domains, respectively.

We also applied our proposed model to study the influence of the rheometer geometry on evaluating the rheological properties of suspensions in a manner akin to the experimental procedure. To do so, we simulated the flow of suspension S1 on three different-sized Couette cells with increasing rotations of the inner cylinder, ranging from 1 to 32 rps, chosen to cover the typical range of applied shear rates in Couette rheometer experiments with suspensions. We calculated the torque values at the rotating cylinder from the simulated velocity fields for all rotation speeds, using them to estimate the rheological parameters m and n of the power-law fluid model, $\tau = 2m\dot{\gamma}^{n-1}\mathbf{E}$. The analytical solution of the equations for the Couette flow of a power-law fluid relates the torque at the inner cylinder to its parameters by:

$$\left. \frac{T_z}{L} \right|_{r=R_i} = -2\pi m \left(\frac{2\omega}{n} \right)^n \left(R_o^{-2/n} - R_i^{-2/n} \right)^{-n}, \tag{43}$$

where T_z is the $z-$component of the torque and L is the length of the rheometer (in the $z-$direction). Since we assumed axial symmetry, only
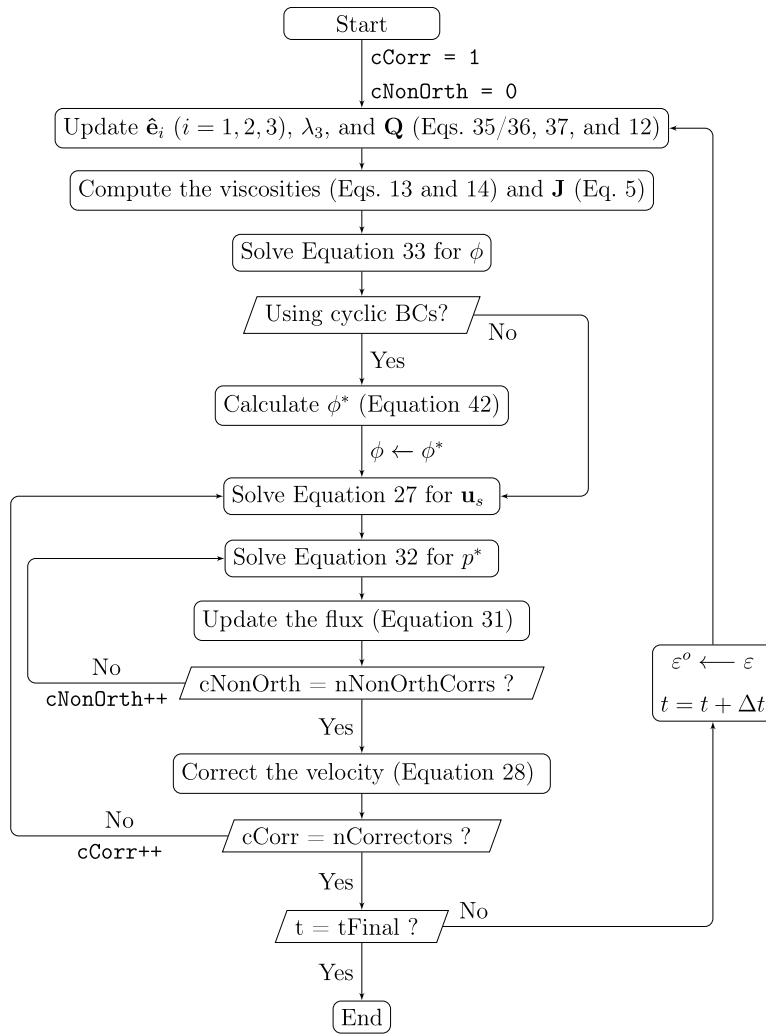
Fig. 1. Solution algorithm for the proposed SBM implemented in OpenFOAM.
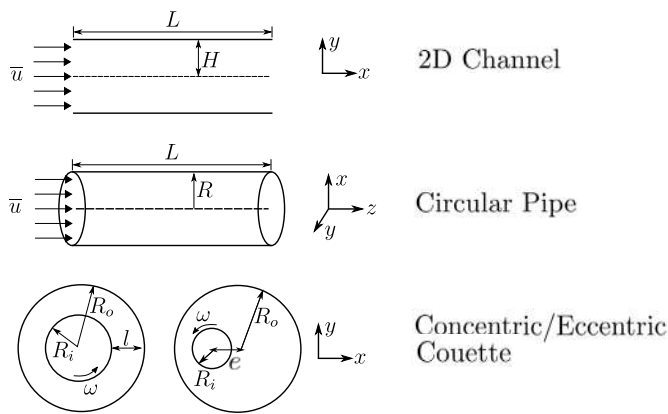

Fig. 2. Schematic description of the configurations of the validation cases. Inlet velocity for Poiseuille flows is represented by $\bar{u}$, and ω is the rotation speed of Couette's inner cylinder.

one layer of cells in the axial direction exists in all employed meshes, whose length is $L = 1$ mm. We estimated parameters m and n using

Orthogonal Distance Regression (ODR) (Boggs et al., 1989), using the grid uncertainty on the torque values to determine the margin of error of the parameters at the 95% confidence level.

Table 4 describes all geometries and computational grids, where geometry A corresponds to the same rheometer of the experimental study of Phillips et al. (1992). Table 5 outlines the boundary conditions for both 1D and 2D simulations. Two pressure–velocity iterations and one non-orthogonal iteration in the correction loops sufficed for all simulations.

4.2. Eccentric Couette flow

For the eccentric Couette flow simulations, we reproduced the experimental setup of Subia et al. (1998) for the eccentricity ratio $\xi = e/(R_o - R_i) = 0.5$, being e the distance between the centre of the cylindrical surfaces that delimit the fluid domain. The outer cylindrical surface with radius $R_o = 2.54$ cm is stationary, and the inner cylinder of radius $R_i = 0.64$ cm rotates at $\omega = 1.5$ rps. In this case, PMMA particles are suspended in a Newtonian fluid of the same density and viscosity of $\mu_f = 4.95$ Pa·s, corresponding to suspension S6 in Table 3. Since the experimental or numerical studies regarding this case (Phan-Thien et al., 1995; Fang and Phan-Thien, 1995; Subia et al., 1998; Mirbod, 2016) did not report the density of the phases, we assumed $\rho_p = 1182$ kg/m^3 as in suspension S1, formed by PMMA particles of the same size.
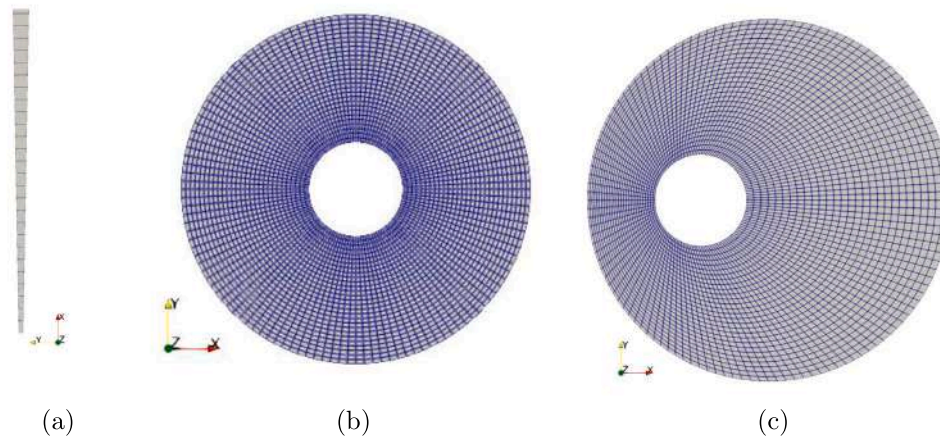
Fig. 3. Coarsest meshes used on the (a) 1D, (b) 2D simulations of Couette flows, and (c) on the simulations of eccentric Couette flows.

Table 4
Description of the Couette geometries and the respective meshes. n_r and n_θ are the number of divisions in the radial and angular directions, respectively, and the total number of cells is given by $N_{total} = n_r n_\theta$.

R_i (cm)	R_o (cm)	$\frac{l}{R_i}$	Simulation type	Geometry & mesh ID	n_r	n_θ	N_{total}
0.64	2.38	2.72	1D	AW1	28	1	28
				AW2	40	1	40
				AW3	56	1	56
0.64	2.38	2.72	2D	A1	28	128	3584
				A2	40	180	7200
				A3	56	256	14 336
1.28	3.02	1.36	2D	B1	28	128	3584
				B2	40	180	7200
				B3	56	256	14 336
1.28	4.76	2.72	2D	C1	40	180	7200
				C2	56	256	14 336
				C3	80	360	28 800

Table 5
Boundary conditions set in OpenFOAM for 1D and 2D simulations of Couette flow.

Patch	$\mathbf{u}_s$	p^*	ϕ
Inner cylinder	$\omega R_i \hat{e}_\theta$	*zeroGradient*	*zeroGradient*
Outer cylinder	*noSlip*	*zeroGradient*	*zeroGradient*
Top and bottom[a]	*wedge*	*wedge*	*wedge*
Front and back	*empty*	*empty*	*empty*

[a] Top and bottom patches only exist for the one-dimensional grids.

Mirbod (2016) reported that the flow achieves a steady state after 10,000 revolutions of the inner cylinder. However, we kept our simulations running until 15,000 revolutions to validate this information. We simulated the flow using three structured grids with 3584, 7200, and 14,336 grid cells. Fig. 3(c) shows the coarsest grid. The numerical setup was the same as in the 2D concentric Couette flow simulations, with the boundary conditions given in Table 5.

4.3. Planar Poiseuille flow

We reproduced the experimental setup of Lyon and Leal (1998), consisting of particles of PMMA dispersed in a Newtonian oil (suspension S2). The suspension enters the channel of half-width $H = 0.9$ mm with uniform velocity $\bar{u} = 0.002$ m/s and uniform solid-phase fraction. We performed 1D (cyclic domain) and 2D simulations to verify the correction applied to the phase fraction field in the former, as given by Eq. (42). For the 2D simulations, we chose the length $L = 1000H$ to

ensure that they achieved the fully developed flow. We employed four pressure–velocity iterations in the correction loop, and there were no non-orthogonal corrections for all channel flow simulations since the computational grids were perfectly orthogonal.

We simulated the flow of the same suspension considered for the Couette rheometer case (suspension S1) in three channels of different widths and with a mean inlet velocity of $\bar{u} = 0.02$ m/s. We compared the simulated values for the pressure drop to those calculated using the analytical solution for the flow of a homogeneous power-law fluid:

$$\bar{u} = \frac{n}{2n+1} \left[\frac{1}{m} \left(-\frac{\Delta p}{\Delta L} \right) \right]^{1/n} H^{1+1/n}, \tag{44}$$

using the values of parameters m and n determined from the Couette rheometer simulations.

Table 6 shows the description of all channel geometries, with geometries AL and A corresponding to the experimental study of Lyon and Leal (1998), along with the respective computational grids. Table 7 outlines the boundary conditions for both 1D (cyclic domain) and 2D simulations.

4.4. Poiseuille flow in circular cross-section pipes

Simulations in the circular cross-section pipe reproduced the conditions of the experimental study of Oh et al. (2015), consisting of a suspension of polystyrene spherical particles dispersed in poly-monobutyl ether (PME), corresponding to suspensions S3 to S5 in Table 3. Since these authors observed that the particles compacted at a maximum concentration of 0.64, we have adopted this value as the maximum packing fraction in our pipe flow simulations to make our suspension model compatible with the experiments. The pure PME density is close enough to the particle's density for the suspension to be considered neutrally buoyant, and we have used $\rho = 1050$ kg/m³ for both phases. We assumed that the suspension enters the pipe of radius $R = 3.15$ mm with uniform solid phase fraction and velocity, whose value of $\bar{u} = 0.0005$ m/s yields a volumetric flow rate within the experimental range reported by Oh et al. (2015).

Table 8 outlines all the employed meshes, with Fig. 4 showing the coarsest mesh, and Table 9 gives the applied boundary conditions. Since the non-orthogonality and skewness of these computational grids were more critical than those for the previous cases, we employed six pressure–velocity and two non-orthogonal iterations on the correction loops. This case is the only one for which we adopted the linear scheme as the default in discretising the gradients instead of using the least squares method. As presented in Table 1, the method used to discretise $\nabla \mathbf{u}_s$ remained unchanged.

Table 6

Description of the two-dimensional channel geometries and the respective meshes. n_x and n_y are the number of divisions in the axial and transversal directions, respectively, with the total number of cells given by $N_{total} = n_x n_y$.

H (mm)	L	Suspension ID	Simulation type[a]	Geometry & mesh ID	n_x	n_y	N_{total}
0.9	$1000H$	S2	2D	AL1	1000	50	50 000
				AL2	1400	70	98 000
				AL3	2000	100	200 000
0.9	$H/2$	S2	1D	A1	1	50	50
				A2	1	70	70
				A3	1	100	100
4	$H/2$	S1	1D	B1	1	100	100
				B2	1	140	140
				B3	1	200	200
8	$H/2$	S1	1D	C1	1	200	200
				C2	1	280	280
				C3	1	400	400
12	$H/2$	S1	1D	D1	1	300	300
				D2	1	424	424
				D3	1	600	600

[a] 1D = cyclic domain.

Table 7

Boundary conditions set in OpenFOAM for 1D (cyclic domain) and 2D simulations of two-dimensional channel flow.

Patch	$\mathbf{u}_s$	p^*	ϕ
1D Simulations			
Inlet and outlet[a]	cyclic	cyclic	cyclic
Walls	noSlip	zeroGradient	zeroGradient
Front and Back	empty	empty	empty
2D Simulations			
Inlet	$\bar{u}\hat{e}_x$	zeroGradient	ϕ_{IN}
Outlet	zeroGradient	0	zeroGradient
Walls	noSlip	zeroGradient	zeroGradient
Front and Back[b]	empty	empty	empty

[a] These patches are planes normal to the x direction.

[b] These patches are planes normal to the z direction.

Table 8

Description of the cases for the circular cross-section pipe flow simulations.

Case ID	Suspension ID	Simulation type	N_{total}
A1	S3	2D	2220
A2	S3	2D	4452
A3	S3	2D	6300
A4	S4	2D	6300
A5	S5	2D	6300

Table 9

Boundary conditions set in OpenFOAM for the circular cross-section pipe flow simulations.

Boundary	$\mathbf{u}_s$	p^*	ϕ
Inlet and outlet[a]	Cyclic	Cyclic	Cyclic
Walls	No slip	Zero gradient	Zero gradient

[a] These patches are planes normal to the z direction.

4.5. Estimating the dimensionless parameters

To validate the hypotheses given by Eqs. (1), (2) and (3) for the application of the SBM to our simulated cases, we estimated the Stokes, particles' Reynolds and Péclet numbers from their geometric and flow conditions. We estimated the shear rates for each geometry by the following relations:

$$\dot{\gamma}_{PP} = \frac{3\bar{u}}{2H}, \quad \dot{\gamma}_{CP} = \frac{2\bar{u}}{R}, \quad \dot{\gamma}_{CC} = \frac{\omega R_i}{R_o - R_i}, \quad \dot{\gamma}_{EC} = \frac{\omega R_i}{R_o - (R_i + e)} \quad (45)$$
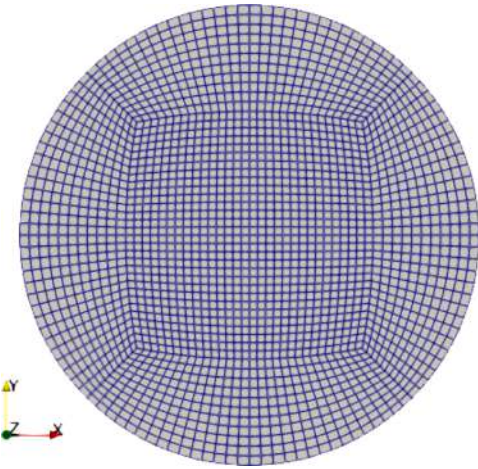

Fig. 4. Coarsest mesh used on the simulations of pipe flow.

where the subscripts PP, CP, CC, and EC correspond to the Poiseuille flow in a two-dimensional channel and a circular tube and the concentric Couette and eccentric Couette flows, respectively.

To also evaluate the Stokes flow hypothesis, we estimated the Reynolds number for the suspension flow in each configuration using the suspension viscosity (Eq. (15) with $\phi = \phi_{IN}$). We applied the following relations:

$$Re_{PP} = \frac{3\bar{u}H\rho_f}{2\mu_s}, \qquad Re_{CC} = \frac{\omega R_i \rho_f (R_o - R_i)}{\mu_s},$$
$$Re_{CP} = \frac{2\bar{u}R\rho_f}{\mu_s}, \qquad Re_{EC} = \frac{\omega R_i \rho_f (R_o - R_i + e)}{\mu_s} \quad (46)$$

Table 10 shows the ranges of the St, Re_p, Pe and Re determined for all studied cases, except for the concentric Couette flow simulations with ω above 2 rps presented in Section 5.5, which discusses them.

The estimates of Pe, Re_p, Pe, and Re shown in Table 10 support the neglect of Brownian motion effects, the assumption of rapid particles' velocity relaxation, inertialess formulation for the particles' drag force, and the suspension flow in the Stokes regime.

5. Results and discussion

To assess each of the proposed modifications to the SBM, including the improvement in the momentum interpolation method, Table 11

Table 10

Estimated ranges for the dimensionless Stokes, particle's Reynolds, Péclet and Reynolds numbers, determined using Eqs. (1), (2), (3) and (46) with the shear rates estimated by Eq. (45).

	St	Re_p	Pe	Re
Minimum	4.84×10^{-8}	4.54×10^{-7}	1.80×10^{9}	9.20×10^{-5}
Maximum	1.13×10^{-5}	1.07×10^{-4}	1.25×10^{13}	3.51×10^{-2}

Table 11

Identification of the different SBM solvers used in our simulations according to the selected models for the unit vectors $\hat{\mathbf{e}}_i$, $\mathbf{S}_p^n$ and momentum interpolation.

Solver ID	$\hat{\mathbf{e}}_1, \hat{\mathbf{e}}_2, \hat{\mathbf{e}}_3$	$\mathbf{S}_p^n$	Momentum interpolation
I	Constant	Eq. (11)	Rhie and Chow (1983)
II	Eq. (36)	Eq. (18)	Section 3.1
III	Eq. (36)	Eq. (16)	Section 3.1
IV	Eq. (36)	Eq. (11)	Section 3.1
V	Eq. (35)	Eq. (18)	Section 3.1
VI	Eq. (35)	Eq. (18)	Rhie and Chow (1983)
VII	Eq. (24)	Eq. (18)	Section 3.1

Table 12

Comparison of the computational costs for the 1D and 2D channel flow simulations using Solver II.

Simulation ID	Used processors	Execution time	Execution time ratio[a]
A1	1	2.9 min	146.8
AL1	6	7.1 h	
A2	1	6.2 min	361.9
AL2	16	37.4 h	
A3	1	14.1 min	518.3
AL3	24	121.8 h	

[a] (Long channel execution time)/(Cyclic channel execution time).

lists the different combinations of the formulations for the anisotropic tensor $\mathbf{Q}$, particles' normal stress $\mathbf{S}_p^n$, and momentum interpolation method. Solver V corresponds to the final proposed model for 2D and 3D simulations, with our modified calculation of the anisotropic tensor, our local formulation of the extra stress and the improved momentum interpolation. Solver II is Solver V applied to two-dimensional planar Poiseuille flow. In addition to the SBM solvers outlined in Table 11, we also perform simulations using a two-fluid model solver (Municchi et al., 2019a), corresponding to the model described in the work of Municchi et al. (2019b), identified as "TFM solver".

All results presented from now on are identified by the Solver ID and by the geometry and mesh ID. We assured grid convergence for all considered cases, using Solver II for channel flow simulations and Solver V for the Couette and pipe flow simulations. Appendix A presents the results for the uncertainties in the intermediate and fine meshes and the observed order of accuracy. The only exception is for simulations using Solver IV, which did not converge. We discussed this behaviour when analysing the extra stress formulations in Section 5.3.2.

5.1. Verification of the cyclic domain formulation

Municchi et al. (2019b) presented results for the 1D and 2D simulations of the same planar Poiseuille suspension flow using the two-fluid model, which do not coincide, exhibiting a clear difference in mass conservation. This discrepancy was probably due to the direct usage of OpenFOAM's periodic boundary condition (*cyclic*) in the 1D simulation of the fully developed flow without keeping constant the mass flow rate average of the dispersed-phase fraction. As shown below, we solved this issue by correcting the phase fraction field according to Eq. (42) at every time step.

Fig. 5 shows the results of simulations performed using the 1D simplification (cyclic domain) of the two-dimensional straight channel using the cyclic boundary condition together with the correction given by Eq. (42) (A3), and using the 2D long channel simulations (AL3), both performed with Solver II. We normalised the dispersed-phase fraction profiles by ϕ_m and the axial velocity profiles by the theoretical maximum velocity of a pure Newtonian fluid (V_{max}). The maximum difference between the phase fraction and velocity results are 0.09% and 0.25%, respectively, within the estimated grid uncertainties. Thus, we considered the results to be equivalent. Fig. 5 shows the results for the finer grids, but the simulations on the intermediate and coarse meshes showed the same behaviour.

The main advantage of using the cyclic domain approach is reducing the computational effort needed to simulate a fully developed duct flow. We compared the execution time of both simulation types for the pairs of equivalent grids, A1/AL1, A2/AL2, and A3/AL3, which have

the same number of divisions in the transversal direction. We ran the 1D and 2D simulations on each pair of equivalent grids on the same computer using dedicated processors of a cluster node. The execution time reported by OpenFOAM is the CPU time of the master process in the MPI processor pool. Therefore, it represents the turnaround time to get the simulation results. Table 12 compares the execution times for the 1D and 2D simulations, giving their ratio. As the number of grid cells dramatically increases with the mesh refinement, so does the number of processors used in the 2D simulation to make its execution time feasible. We did not engage in a detailed parallelisation study to determine the ideal number of processors for each simulation. However, the ratios of execution times show the clear advantage of using the periodic boundary conditions in the simplified geometry to simulate the fully developed flows at the steady state. Using cyclic domains allowed us to extensively simulate channel and pipe flows using the solvers listed in Table 11 for several conditions. Unless stated otherwise, the following 2D channel and pipe flow results were obtained using cyclic domains.

5.2. Evaluation of the improved momentum interpolation method

To implement the frame-invariant formulation of the anisotropic stress tensor, we started our development from Solver I, corresponding to the work of Dbouk et al. (2013a). Since it is a frame-dependent solver, it performs simulations with the anisotropic tensor $\mathbf{Q}$ formulation given by Eq. (12) with constant unit vectors coinciding with OpenFOAM's reference coordinate system, which is the Cartesian frame of reference. Thus, Couette flow simulations employed the 1D simplified domain presented in Fig. 3(a) using OpenFOAM's *wedge* boundary conditions to impose symmetry in the θ−direction. Because it is a perfectly orthogonal grid, the unit vectors describing the Couette flow in cylindrical coordinates, which are $\hat{\mathbf{e}}_1 = \hat{\mathbf{e}}_\theta$, $\hat{\mathbf{e}}_2 = \hat{\mathbf{e}}_r$ and $\hat{\mathbf{e}}_3 = \hat{\mathbf{e}}_z$, can be represented by the Cartesian unit vectors, namely $\hat{\mathbf{e}}_1 = \hat{\mathbf{e}}_y$, $\hat{\mathbf{e}}_2 = \hat{\mathbf{e}}_x$ and $\hat{\mathbf{e}}_3 = \hat{\mathbf{e}}_z$.

Fig. 6(a) compares the results obtained with Solvers I, V and VI for the particles' phase fraction and velocity profiles for the steady-state Couette flow. This figure shows that Solver VI gave the particles' phase fraction field with numerical oscillations, especially near the outer cylinder. On the other hand, Solver V yielded results without oscillations that were equivalent to those generated by Solver I. Although Solvers V and VI employ our formulation of the anisotropic stress tensor, the latter uses the standard momentum interpolation method, whereas the former applies the improved momentum interpolation method. This result not only supports the correctness of our implementation of the $\mathbf{Q}$ calculation using Eq. (35), but also the adequacy of the proposed particles' stress tensor model (Eqs. (18) and (19)) for Couette flows.

For Solver V results, we also verified that λ_3 stayed constant and equal to 0.5 throughout the domain and that $\hat{\mathbf{e}}_3$ was always calculated using the curl of the velocity field, which we expected as there is no plateau region in the Couette flow.
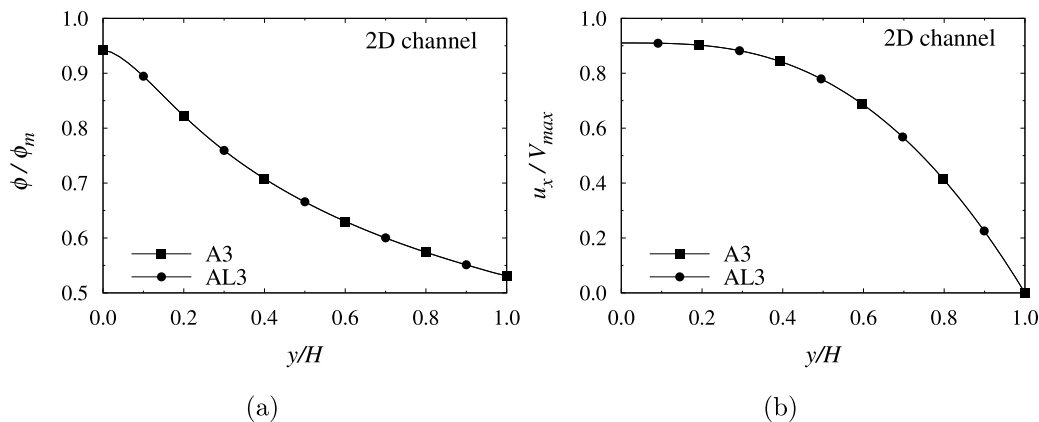
Fig. 5. Comparison of the steady-state fully developed flow profiles for the (a) solid-phase fraction and (b) dimensionless axial velocity obtained for the one-dimensional (using the cyclic domain) and two-dimensional simulations of the planar Poiseuille 2D channel flow of suspension S2 using Solver II.
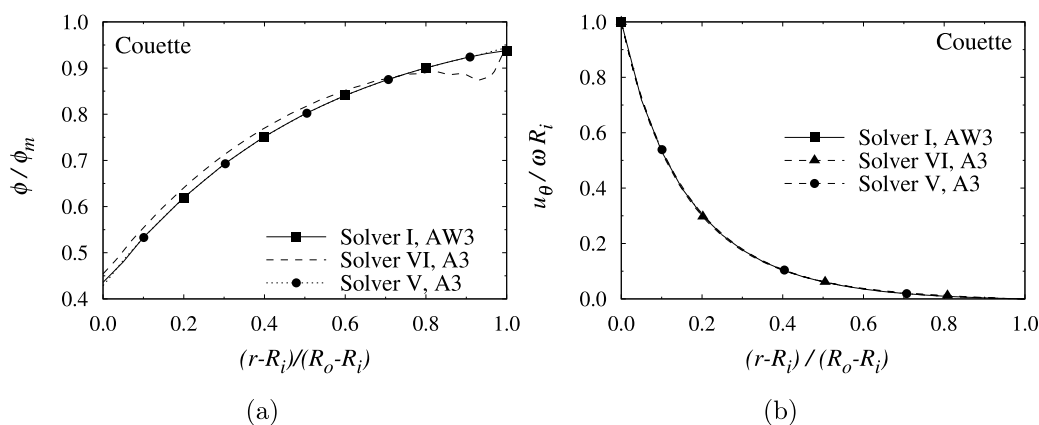

Fig. 6. Comparison of the steady-state (a) dispersed-phase fraction and (b) dimensionless angular velocity profiles obtained with different formulations of the SBM for Couette flow.

5.3. Evaluation of the new stress tensor model

5.3.1. New anisotropic stress tensor formulation

To illustrate the expected components of $\mathbf{Q}$ using its conceptual definition given by Eq. (12) and the directions of $\hat{\mathbf{e}}_i$, $i = 1, 2, 3$ described after it, consider the steady-state and fully developed suspension flow in a cylindrical pipe with a circular cross-section, for which the directions of the velocity, its gradient, and vorticity in cylindrical coordinates are $\hat{\mathbf{e}}_z$, $\hat{\mathbf{e}}_r$, and $\hat{\mathbf{e}}_\theta$, respectively. By transforming a coordinate system from cylindrical to Cartesian coordinates, we calculated the non-zero components of $\mathbf{Q}$ shown in Fig. 7. Appendix B gives details of this coordinate transformation.

Fig. 8 demonstrates the motivation behind calculating the anisotropic stress tensor by Eq. (35). It shows the five non-zero components of $\mathbf{Q}$ obtained for pipe flow simulation A3 using the local coordinate system defined by Eq. (24) (Solver VII). Comparing the expected values of the $\mathbf{Q}$ components given in Fig. 7 to those shown in Fig. 8, we observe strong non-physical deviations from the expected values of the $\mathbf{Q}$ components in the central region of the duct, which are oscillatory in both space and time. These perturbations arise due to the intrinsic inaccuracy in determining $\hat{\mathbf{e}}_3$ using Eq. (24) in regions where $\|\nabla \times \mathbf{u}_s\|$ is close to zero. Since the direction of $\hat{\mathbf{e}}_3$ varies at every time step, and so do the components of $\mathbf{Q}$, the simulation never reaches a steady-state solution.

Fig. 9 shows the same $\mathbf{Q}$ components obtained using Solver V with our proposed formulation of the anisotropic stress tensor. All components that depend on λ_2 and λ_3 (Figs. 9(a)–9(c)) feature two distinct regions separated by a smooth yet thin transition layer. In the

central region, $\lambda_2 = \lambda_3$. In the outer region, they follow the expected pattern presented in Fig. 7. The simulations converged to a steady-state result with constant components of $\mathbf{Q}$. Still, there are perturbations at $\theta = \pm n\pi/4$ ($n = 1, 3$) due to the higher mesh non-orthogonality and skewness at this transition region from a fully orthogonal grid in the central block of the O-grid mesh to the mesh blocks adjacent to the duct wall (see Fig. 4). For this reason, We always evaluated line plots for pipe flows at $\theta = \pi/2$.

Fig. 10 shows the λ_3 and κ profiles obtained from pipe flow simulation A3 using Solver V and the calculated value of $\kappa_0 = 0.116$. The transition region of λ_3 from 0.8 to 0.5 takes about 10% of the radial coordinate interval, with the intersection between κ and κ_0 accurately marking its midpoint.

5.3.2. Extra stress contribution

Fig. 11 displays the results for evaluating the different models for the extra stress in terms of the dispersed-phase fraction profiles obtained for the two-dimensional straight channel flow simulations.

In this figure, the solid lines represent the simulation results using Solver IV without adding an extra stress term to the particles' normal stress tensor. Even though this case corresponds to the one with a diverging derivative $d\phi/dy$ at the channel's central plane, the simulations did converge because the numerical error led to a non-zero shear rate at the central plane, preventing the simulations from diverging. However, the solutions of the linear systems composed of the discretised equations did not fully converge for the stipulated tolerance criteria. The zoomed area of Fig. 11 shows that the particles' phase fraction profiles obtained using Solver IV still change significantly with
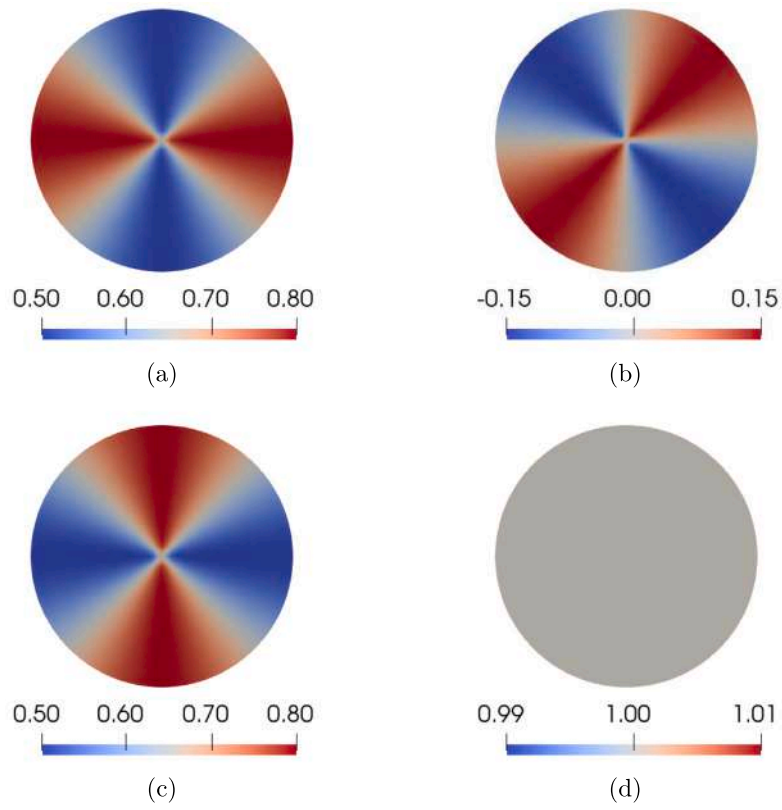
Fig. 7. Components of the anisotropic tensor **Q** for cylindrical pipe flow obtained theoretically from Eq. (12), using constant $\hat{\mathbf{e}}_1$, $\hat{\mathbf{e}}_2$ and $\hat{\mathbf{e}}_3$: (a) Q_{xx}, (b) $Q_{xy} = Q_{yx}$, (c) Q_{yy} and (d) Q_{zz}.
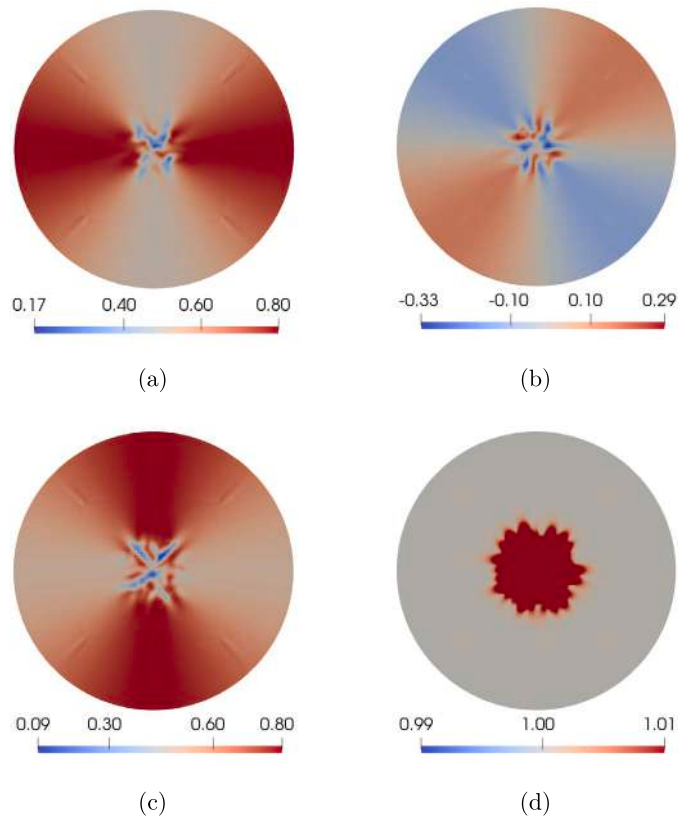

Fig. 8. Simulated components of **Q** at $t = 1000$ s for the pipe flow simulation A3 using Solver VII, with $\hat{\mathbf{e}}_1$, $\hat{\mathbf{e}}_2$ and $\hat{\mathbf{e}}_3$ calculated from Eq. (24): (a) Q_{xx}, (b) $Q_{xy} = Q_{yx}$, (c) Q_{yy} and (d) Q_{zz}.
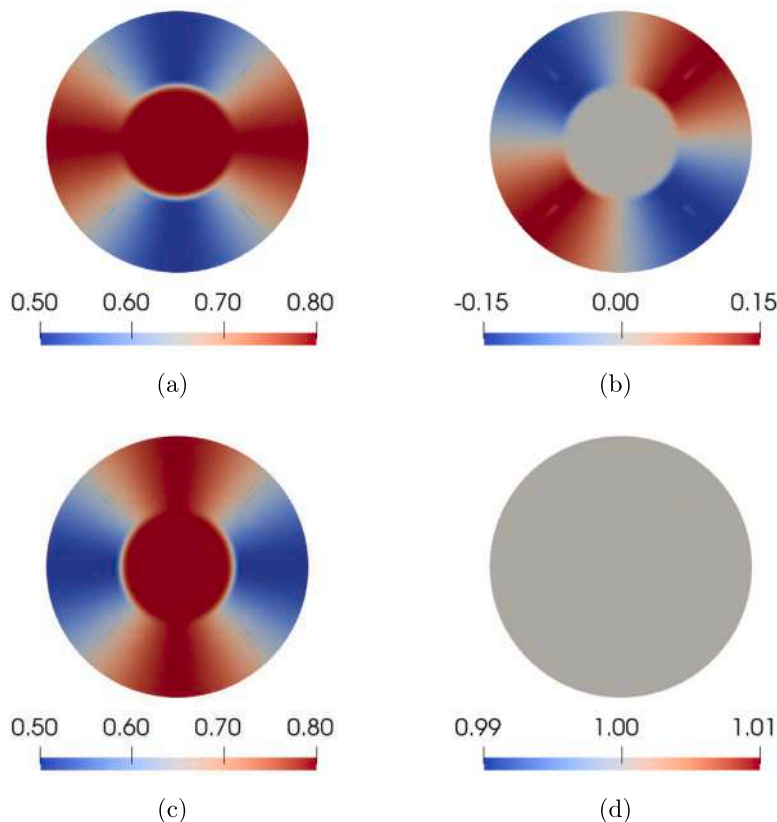
Fig. 9. Simulated components of the anisotropic tensor **Q** at the steady state for the pipe flow simulation A3 using Solver V, with $\hat{\mathbf{e}}_1$, $\hat{\mathbf{e}}_2$ and $\hat{\mathbf{e}}_3$ calculated using Eq. (35) and λ_3 from Eq. (37): (a) Q_{xx}, (b) $Q_{xy} = Q_{yx}$, (c) Q_{yy} and (d) Q_{zz}.
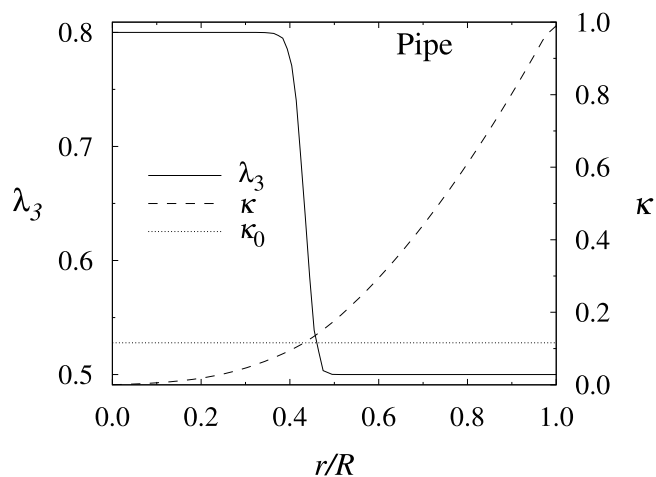
Fig. 10. Steady-state radial profiles for the parameter λ_3, calculated using Eq. (37), and for the κ, used in the transition criterion, obtained from pipe flow simulation A3 using Solver V.

grid refining, indicating poor grid convergence. Simulations performed in an even finer grid ($n_y = 200$) diverged because the calculated values for the shear rate and particles' phase fraction were too close to zero and to ϕ_m, respectively.

The dashed lines in Fig. 11 represent the results obtained using Solver II, with our proposed formulation of the extra stress, using $k = 10^{-3}$ in Eq. (19). This value of k always yielded satisfactory results for our planar Poiseuille and Couette flows simulations. In contrast

to the simulations using Solver IV, the solution of the linear systems converged, and there was grid convergence. Simulations of this flow in even finer grids ($n_y = 200$, 400) also converged and yielded the same phase-fraction field obtained for grid A3.

The extra stress term acts against the migration of particles towards the centre line, playing the role of a repulsive force that prevents the suspension from jamming. The extra stress reaches its maximum value at the centre and its minimum value at the channel walls. For comparison, Fig. 11 also shows the results obtained using Solver III at the finest grid (A3), which uses the constant non-local correction of Miller and Morris (2006).

5.4. Validation of the proposed model

Using the final implementations for 1D (Solver II) and 2D (Solver V) simulations, we validate our model against experimental and literature data.

Fig. 12 presents the results for the dispersed-phase fraction and dimensionless velocity profiles for the fully developed flow in the two-dimensional straight channel. We show in Fig. 12(a) the results of the TFM-1D and TFM-2D simulations, obtained by Municchi et al. (2019b), which are significantly different due to the lack of the correction of the solid phase fraction field when using the periodic boundary conditions. The results of the 1D simulation using the original SBM, reproduced from Dbouk et al. (2013a) (SBM-1D), are almost identical to those obtained in the 2D simulation of Municchi et al. (2019b), reinforcing the idea that the simplification of the system as one effective fluid is capable of accurately representing the mixture flow. Our results using Solver II slightly differ from those, especially at the centre of the channel. However, differences among these results are within the experimental error range. Unfortunately, the referred studies do not
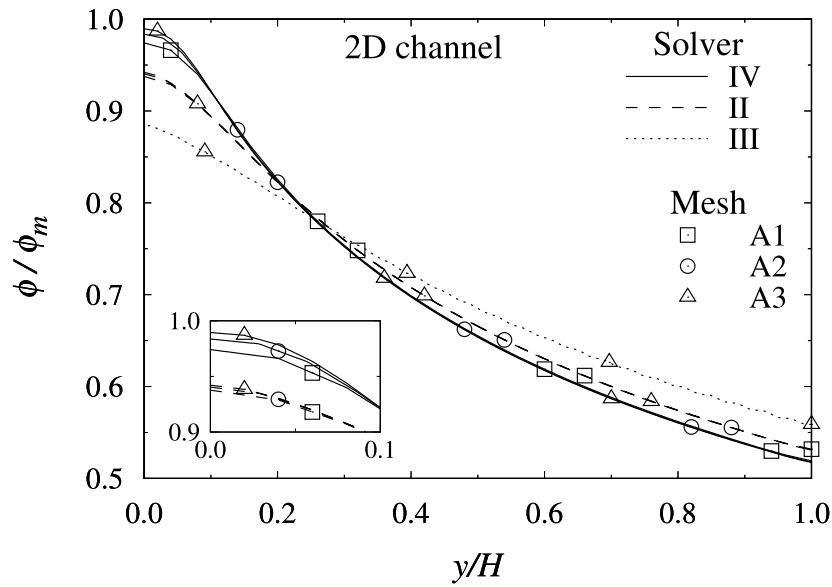
Fig. 11. Grid convergence of the dispersed-phase fraction profiles using different formulations for the extra stress term (Solvers II, III and IV using suspension S2).
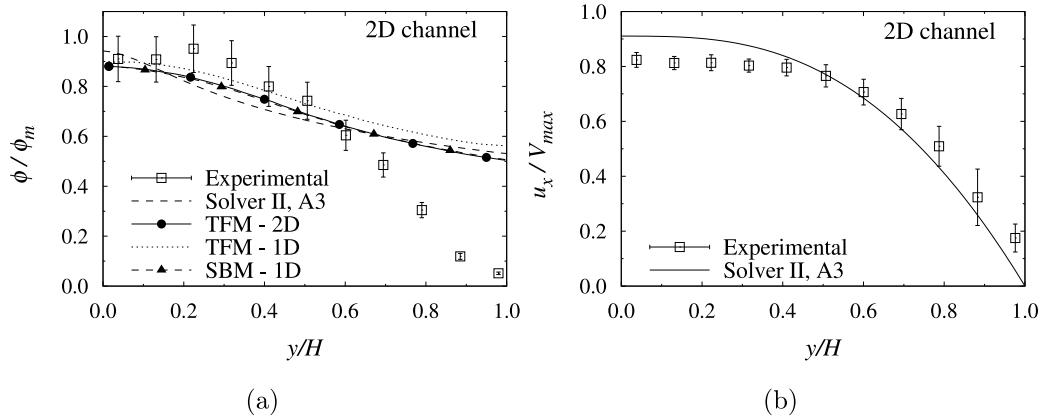

Fig. 12. Comparison of the steady-state fully developed flow of suspension S2 in a 2D channel considering the profiles of the (a) dispersed-phase fraction and (b) dimensionless velocity profiles obtained using Solver II, the experimental data from Lyon and Leal (1998), the TFM results from Municchi et al. (2019b), and the SBM results from Dbouk et al. (2013a).
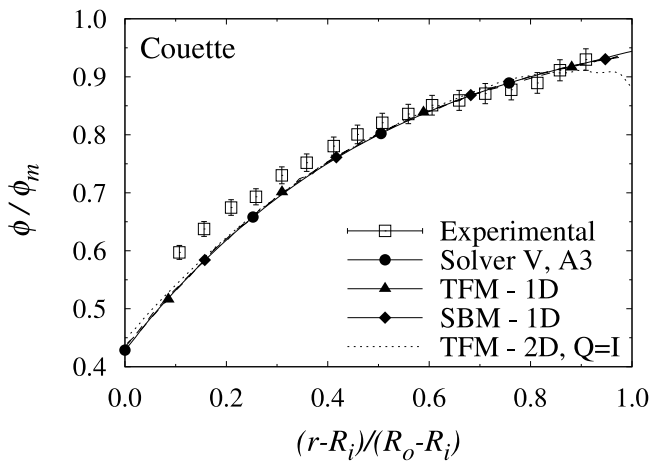
Fig. 13. Comparison of the steady-state dispersed-phase fraction profile obtained for Couette flow using suspension S1 and Solver V with the experimental data from Phillips et al. (1992) and literature data. TFM - 1D results were extracted from Municchi et al. (2019b), SBM - 1D results from Dbouk et al. (2013a), and TFM - 2D results from Inkson et al. (2017).

provide the respective velocity profiles.

As for Couette flow simulations, the particles' phase fraction profiles presented in Fig. 13 show that our final model (Solver V) provides the same results as the original SBM (Dbouk et al., 2013a) (SBM-1D) and the TFM (Municchi et al., 2019b) (TFM-1D) simulations, both obtained using the 1D simplification of the Couette geometry with constant anisotropic tensor formulation. Particularly, for the Couette flow under analysis, there is no region in the flow domain with $\kappa < \tau$. Therefore, the calculation of the unit vectors $\hat{\mathbf{e}}_i$ by Eq. (35) is equivalent to using Eq. (24) with constant λ_3. This observation confirms the correct implementation of our proposed model and its ability to represent generic 2D flows for which no correction in the calculation of $\hat{\mathbf{e}}_3$ and λ_3 is needed due to the absence of regions of constant or near-constant velocity.

Solver V results for the dispersed-phase fraction are essentially equal to those of SBM-1D and TFM-1D simulations. This observation and the analysis presented in Section 5.3.2 reinforce the conclusion that one can apply the proposed extra stress contribution to any flow geometry. This extra stress is part of the particles' stress model, and the magnitude of its effects depends on the flow characteristics. For the Couette flow considered here, even though this contribution is present, it does not significantly alter the steady-state results of the simulation.

Fig. 14. Streamlines for the eccentric Couette flow (with $\xi = 0.5$) at the steady state obtained using Solver V.

Fig. 15. Comparison of the dispersed-phase fraction profile obtained using Solver V with the SBM simulation results of Mirbod (2016) (steady-state results at 10,000 revolutions), the DFM simulation results of Subia et al. (1998) (after 6000 revolutions) and the experimental data of Subia et al. (1998) (after 10,000 revolutions).

Fig. 13 also shows the results obtained by Inkson et al. (2017) (TFM-2D, Q=I), who used a two-fluid model to simulate the flow in a 2D Couette geometry. However, they neglected the anisotropy of the normal stresses and replaced **Q** with the constant identity tensor **I**. Consequently, they obtain a different concentration profile. We showed in the Supplementary Material that the particles' phase fraction profile depends on the values of λ_1 and λ_2 by analysing the resulting equation for the migration flux for Couette flows. Inkson et al. (2017) observed a slight dependence of the steady-state concentration profiles with the rotation speed of the inner cylinder, which is in disagreement with experimental observations and with the expected SBM behaviour since dimensional analysis can show that the particles' phase fraction profile is independent of the applied shear rate (Fernandes, 2003). Besides, in their simulations using $\phi_m = 0.68$, these authors observed that the particles moved away from the outer cylinder wall, preventing the concentration profile from achieving values above 0.60. They arbitrarily increased the value of ϕ_m for suspension S1 from 0.68 to 0.72 to allow the concentration profile to reach higher ϕ values, obtaining the results presented in Fig. 13. These results also show numerical oscillations near the outer wall. We did not observe such problems in any of our 2D simulations.

To further demonstrate the ability of our model (Solver V) to simulate suspension flow in more complicated geometries, we simulated the eccentric Couette flow for an eccentricity ratio of $\xi = 0.5$. We compared the velocity and concentration fields after 10,000 and 15,000 revolutions of the inner cylinder and observed essentially the same results. Hence, we report steady-state results at 10,000 revolutions of the inner cylinder.

For $\xi = 0.5$, a slow recirculating flow region arises in the wider portion of the gap, as shown in Fig. 14, in agreement with the experimentally observed behaviour (Phan-Thien et al., 1995; Subia et al., 1998).

Fig. 15 compares our results for the dispersed-phase fraction profile over a horizontal line passing through the centre of both cylindrical surfaces with the DFM simulations and experimental data of Subia et al. (1998) and the SBM simulations of Mirbod (2016). In our simulations, there is an abrupt increase in the dispersed phase fraction at the surface of the inner cylinder on the narrow side of the gap. To interpret this behaviour, we present the divergence of the migration flux **J** at this region in Fig. 16. Recalling Eq. (4) for the dispersed-phase fraction, we see that negative values of $\nabla \cdot \mathbf{J}$ represent a source term and positive values of $\nabla \cdot \mathbf{J}$ represent a sink term. In the narrower gap, $\nabla \cdot \mathbf{J}$ close to the inner cylinder is positive when the flow approaches the smallest cross-flow area and eventually becomes negative. This region with negative
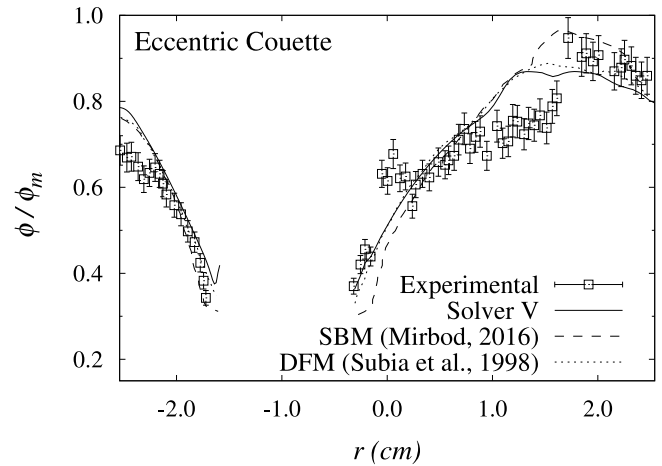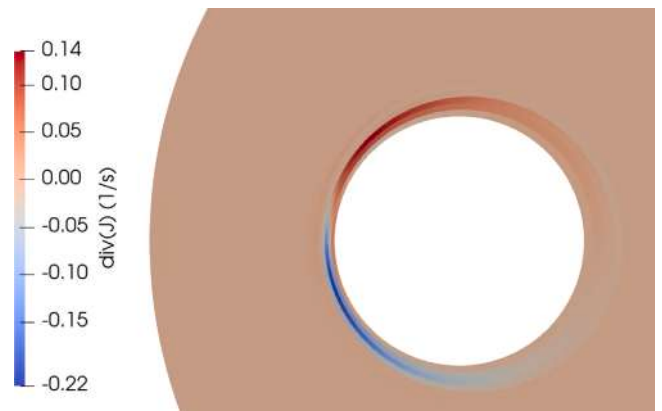

Fig. 16. Divergence field of the migration flux **J** for the eccentric Couette flow (with $\xi = 0.5$) at steady state obtained using Solver V.

values of $\nabla \cdot \mathbf{J}$ is responsible for the local increase on the dispersed-phase fraction observed in Solver V simulation.

Overall, there is a good qualitative agreement among the dispersed-phase fraction profiles shown in Fig. 15. In the three simulations, the point of maximum particle concentration is displaced from the outer cylinder wall towards the recirculating flow region, and quantitative differences may be due to the different modelling strategies. There is an apparent difference in the dynamics of the migration process using the different models. The DFM results reported by Subia et al. (1998) seem to reach the steady state after 6000 revolutions of the inner cylinder, in contrast to both simulations using the SBM that achieved the steady-state results at 10,000 revolutions of the inner cylinder.

The SBM formulation of Mirbod (2016) considered no extra stress in the stress model. Even though this author mentioned using the values of λ_i proposed by Morris and Boulay (1999), she did not specify how she determined the directions of the unit vectors $\hat{\mathbf{e}}_i$. While the anisotropic tensor **Q** main directions are constant for concentric Couette flows using the cylindrical coordinate system ($\mathbf{Q} = \lambda_1 \hat{\mathbf{e}}_\theta \hat{\mathbf{e}}_\theta + \lambda_2 \hat{\mathbf{e}}_r \hat{\mathbf{e}}_r + \lambda_3 \hat{\mathbf{e}}_z \hat{\mathbf{e}}_z$), this is not the case for eccentric Couette flows because the velocity does not align with a coordinate versor. Hence, a formulation which takes into account the variations in the velocity direction is necessary, such as our proposed model. Fig. 17 presents the non-null components of the anisotropic tensor **Q** obtained in our simulation. Some additional results for the eccentric Couette flow simulations are presented in the

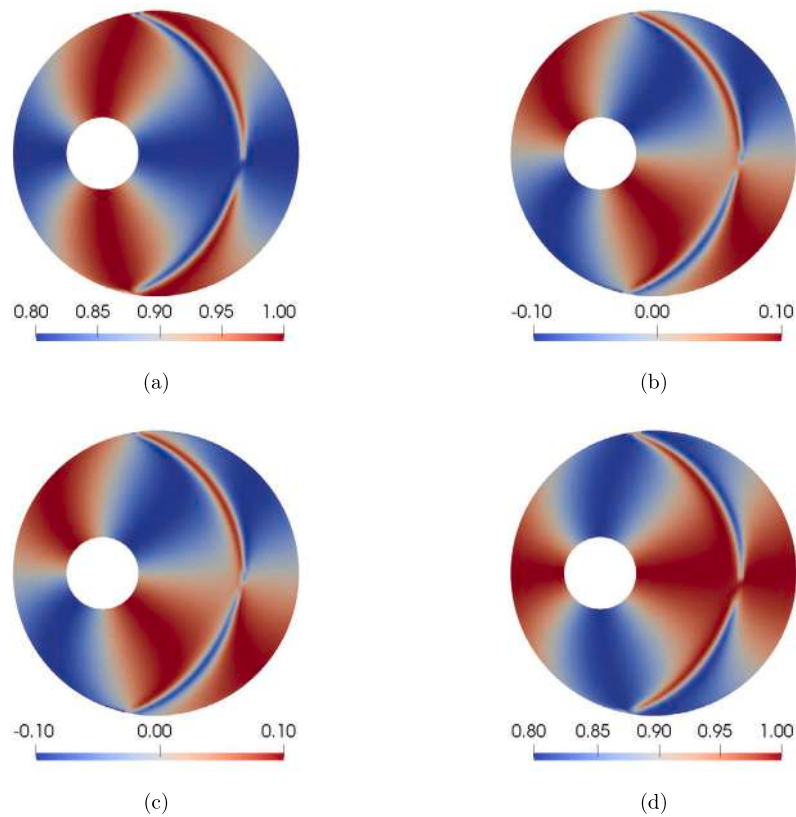**Fig. 17.** Components of the anisotropic tensor **Q** for the eccentric Couette flow (with $\xi = 0.5$) at the steady state (10,000 revolutions) obtained using Solver V: (a) Q_{xx}, (b) Q_{xy}, (c) Q_{yx} and (d) Q_{yy}.

Supplementary Material.

For pipe flow simulations, we reevaluated the value of the parameter k in Eq. (19) and found the optimum value to be $k = 2.0 \times 10^{-5}$. For k lower than 2.0×10^{-5}, the extra shear rate $\dot{\gamma}_e$ is too small to prevent the simulation from diverging. Figs. 18(a) and 18(b) show the dispersed-phase fraction and dimensionless velocity profiles obtained from simulation of case A3 (suspension S3, $\phi_{IN} = 0.55$), with the velocity profiles normalised by the inlet velocity of the suspension, $\bar{u}$. Even though we have plotted the results obtained using the TFM solver, this simulation does not fully converge to a steady-state solution because it employs Eq. (24) for the calculation of the unit vectors $\hat{\mathbf{e}}_i$, and the resulting components of tensor **Q** exhibit an oscillatory and non-physical behaviour similar to that previously shown in Fig. 8. These oscillations in the tensor **Q** components resulted in an oscillation around 1% for the phase-fraction profile at every 10 seconds.

Fig. 18 also shows that the results obtained using Solver V successfully capture the qualitative behaviour of the experimental data, featuring a jammed region with constant dispersed-phase fraction and velocity at the centre of the pipe. Our model, however, underpredicts the extent of both regions. Oh et al. (2015) also observed an underprediction on the size of this central plug-flow-like region when comparing their experimental data to the predictions using a frictional rheology model. The experimental data suggest a stronger migration than both models' predictions, with a smaller concentration at the pipe walls and a larger jammed region. Consequently, the experimental velocity profile is more blunted than our model predicts.

Fig. 19 shows similar results for simulations of cases A4 and A5, corresponding to suspensions S4 and S5, respectively. For the flows of these more dilute suspensions, which do not achieve the maximum value of the dispersed-phase fraction, agreement with the experimental data increases significantly, with the predicted and experimental velocity profiles matching almost perfectly for suspension S5. For both

simulations, there is still a region at the centre of the pipe with $\kappa < \tau$ in which the solver modifies the calculation of tensor **Q**. As the bulk concentration of the suspension decreases, so does the size of this region. Simulations of cases A4 and A5 using the TFM solver diverged.

Attempting to apply our proposed model to more complicated flows, we simulated suspension flow in a pipe with an abrupt expansion (1:4 expansion ratio) using Solver V. Such flows feature high-velocity gradients at the expansion due to the sudden change in the cross-sectional area and a recirculation region where the flow transitions from simple shear to extensional flow. Our model could not reproduce experimental (Moraczewski et al., 2005) or simulation results obtained using a more sophisticated stress model (Badia et al., 2022) for the length of the recirculation zone. Therefore, the application of our model should be limited to shear-dominated flows, such as those we presented above. Details of the studied flow with an abrupt expansion and the obtained results are given in the Supplementary Material.

5.5. Estimation of rheological parameters

This section focuses on the consequences of describing the suspension rheology as a pseudo-homogeneous non-Newtonian fluid. To do so, we used the results from our flow simulations in three different Couette viscometers (numerical experiments) to adjust a rheological model to the simulated shear stress. Then, we tested the adjusted rheological model to predict the behaviour of the same suspension in a planar Poiseuille flow.

We performed Couette flow simulations of suspension S1 in geometries A3, B3 and C3 using our final model (Solver V) for inner cylinder rotations starting from $\omega = 1$ rps and duplicating the angular velocity until the low Reynolds assumption was no longer valid. For $\omega = 32$ rps, despite observing maximum values of $Re_p = 2.11 \times 10^{-3}$
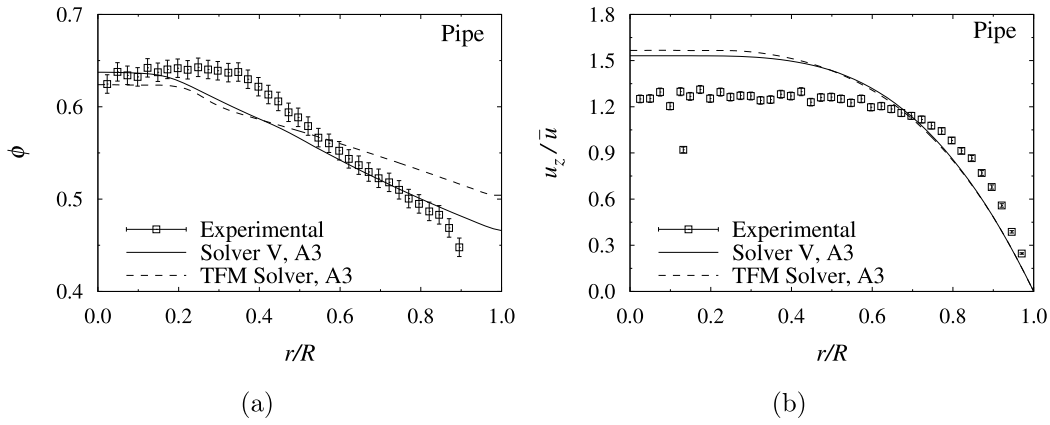
Fig. 18. Comparison of the steady-state fully developed profiles of the (a) dispersed phase-fraction and (b) velocity profiles obtained in our cylindrical pipe simulations (case A3, $\phi_{IN} = 0.55$) using Solvers V and the TFM Solver, and the experimental data of Oh et al. (2015).
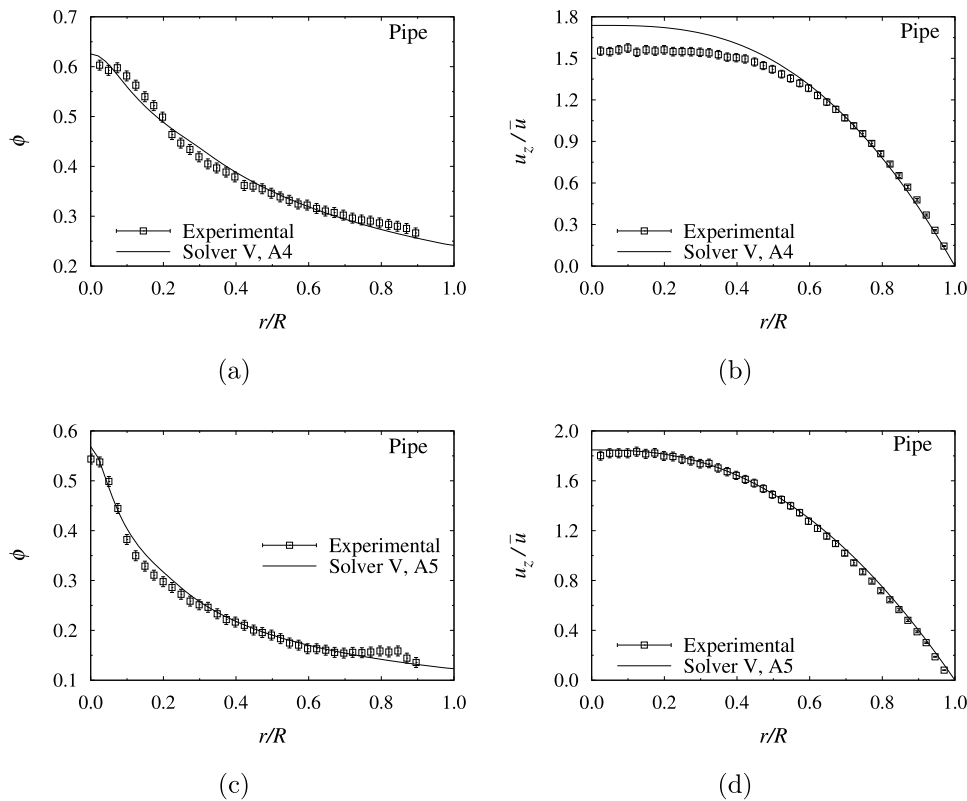
Fig. 19. Comparison of steady-state fully developed profiles for the dispersed phase-fraction (left) and dimensionless velocity profiles (right) obtained in our pipe flow simulations of cases A4 ($\phi_{IN} = 0.35$) (a and b) and A5 ($\phi_{IN} = 0.20$) (c and d) using Solver V, together with the experimental data of Oh et al. (2015).

and $St = 2.24 \times 10^{-4}$ for all geometries, the suspension flow Reynolds number reached $Re = 1.12$ in geometry C3. Hence, we did not increase ω any further.

For each studied geometry, steady-state results for the dispersed-phase fraction and velocity fields were independent of the inner cylinder's rotation speed, suggesting a Newtonian response to the sheared suspension. Fig. 20 shows the steady-state results obtained for the different rheometer sizes, showing that simulations using geometries A and C led to equivalent results, which are, in turn, different from those obtained for geometry B. This observation shows that the ratio l/R_i dictates the similarity of the segregation profiles between two distinct rheometers, which is the same for geometries A and C (see Table 4).

Table 13 presents the resulting values for the estimated power-law parameters from Eq. (43). The power coefficient n is close to 1 for all considered geometries, suggesting a Newtonian behaviour of the

suspension. The estimated apparent viscosities are significantly greater than the viscosity of the continuous phase, $\mu_f = 9.45$ Pa·s, and do not match the values calculated assuming a pseudo-homogeneous fluid with concentration ϕ_{IN} and shear viscosity given by Eq. (15), which yields $\mu_s (\phi = \phi_{IN}) = 94.3$ Pa·s. These results show that different apparent viscosities are obtained for the same suspension flowing in different geometries when assuming a pseudo-homogeneous rheological model to interpret rheometric experiments.

We also performed simulations of the flow of suspension S1 in the 2D straight channels B3, C3 and D3 using Solver II. The minimum and maximum concentration values, observed at the channel wall and centre line, respectively, were 0.422 and 0.659 for geometry B, 0.426 and 0.652 for geometry C, and 0.430 and 0.646 for geometry D. Since the difference in the channels' widths is smaller than the difference between the Couette gap sizes (millimetres versus centimetres), the
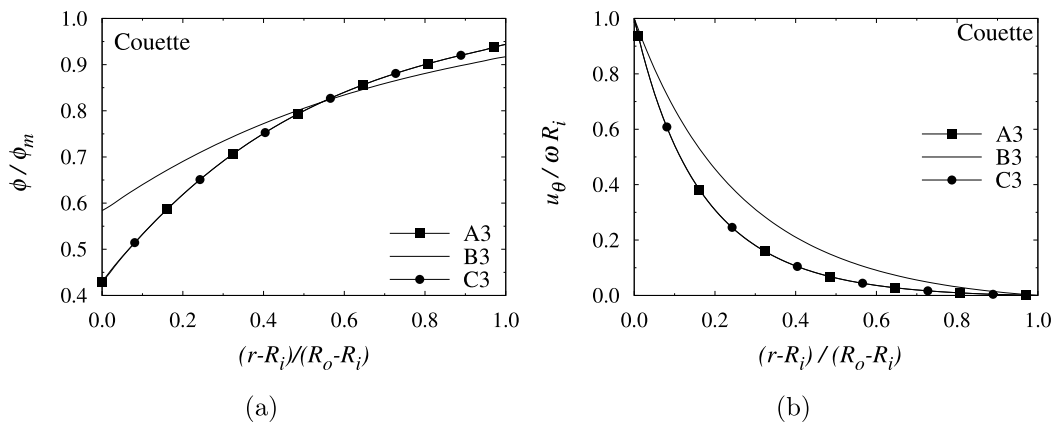
Fig. 20. Steady-state profiles for the (a) dispersed-phase fraction and (b) dimensionless angular velocity obtained for the flow of suspension S1 in different Couette geometries using Solver V.

Table 13
Estimates for the parameters of the power-law model using the simulated results from the Couette flows for suspension S1 in different geometries.

Variable	Geometry		
	A3	B3	C3
m (Pa·s)	$33.8 \pm (4.1 \times 10^{-4})$	$54.6 \pm (1.1 \times 10^{-3})$	$34.4 \pm (6.5 \times 10^{-3})$
n	$1.0 \pm (2.6 \times 10^{-6})$	$1.0 \pm (3.7 \times 10^{-6})$	$1.0 \pm (3.8 \times 10^{-6})$

Table 14
Comparison of the simulated pressure drop values for different 2D channel simulations with the calculated values using the estimated power law model parameters in Eq. (44).

m (Pa·s)[a]		Geometry		
		B3	C3	D3
	Simulated values			
–	$-\Delta p/\Delta L$ (kPa/m)	181.14	46.28	20.93
	Calculated Values			
33.79	$-\Delta p/\Delta L$ (kPa/m)	12.67	3.17	1.41
	Ratio[b]	14.30	14.60	14.84
54.64	$-\Delta p/\Delta L$ (kPa/m)	20.49	5.12	2.28
	Ratio[b]	8.84	9.04	8.90
34.45	$-\Delta p/\Delta L$ (kPa/m)	12.92	3.23	1.44
	Ratio[b]	14.02	14.33	14.53

[a] Value of parameter n is equal to 1 in all calculations.

[b] $Ratio = (\Delta p/\Delta L)_{sim} / (\Delta p/\Delta L)_{calc}$.

difference in the segregation profiles was less significant.

Table 14 shows the simulated pressure drops for the channel flows in geometries B3, C3 and D3, along with the values calculated by Eq. (44) considering the power-law model and using the estimated parameters presented in Table 13. The ratio between the simulated and calculated values ranges from 8.84 to 14.84, reinforcing that the power-law model cannot predict the behaviour of the suspension. It becomes clear that the interpretation of suspension rheological data is not straightforward. Therefore, one must interpret experimental rheometric data using a more sophisticated model rather than simple non-Newtonian models.

6. Concluding remarks

We considerably improved the formulation and implementation of the suspension balance model compared to those of previous works, leading to a frame-independent SBM solver that is stable and robust.

We implemented a solid mass flow rate correction necessary for simulating suspension flows in cyclic domains using the OpenFOAM's periodic boundary condition. This correction was verified, making it possible to obtain results for the steady-state fully developed duct flow in a reasonable execution time. We also presented an improved momentum interpolation method that was applied to a mixture model for the first time to the best of our knowledge, ensuring the robustness of the numerical code. It allowed us to simulate 2D Couette flows with a frame-invariant anisotropic stress tensor without resorting to the 1D simplification, which is an essential step towards the ability to simulate generic flows for which the directions of the flow, its gradient and vorticity change concerning the domain coordinate system.

Our proposed particles' stress model includes a new local formulation of the extra stress associated with the action of the lubrication forces at the particle-size scale. Our extra stress model effectively prevents the simulation from diverging when there is a zero or near-zero shear rate region in the flow, exhibiting good grid convergence. It is an algebraic and geometry-independent extra stress model, in contrast to the currently available formulations which may involve solving additional transport equations (Nott and Brady, 1994) or which are geometry-dependent (Miller and Morris, 2006).

Our model also includes a physically based non-uniform formulation of the anisotropic stress tensor **Q** that addresses, for the first time, the lack of definition of its main directions in regions of constant or near-constant velocity. This new formulation of **Q** allowed us to accurately simulate circular cross-section pipe flows. We were also able to simulate eccentric Couette flows, for which a formulation taking into account changes in the directions of the velocity and its gradient is necessary.

Using the simulation results for Couette rheometers of different geometries, we performed the rheological characterisation of the suspension similarly to the experimental procedure, always obtaining Newtonian behaviour for the same suspension but with an apparent viscosity that depends on the rheometer geometry. Flow simulations in two-dimensional straight channels showed that, when using the parameters estimated from the Couette rheometer simulations to calculate the pressure drop in the channel, the resulting values are underestimated up to 15 times compared to the SBM predictions.

Application of our proposed model is limited to flows in the Stokes regime with negligible particle inertia and Brownian motion. It is also limited to shear-dominated flows, for which it was extensively validated. Simulations of the suspension flow through an abrupt expansion showed that the model cannot be directly extended to flows with more complex kinematics. Despite those limitations, extending our SBM implementation to flows outside the Stokes regime by including the inertial terms in the suspension flow momentum equation is straightforward. Moreover, all our developments implemented for the SBM are easily adaptable for an Euler–Euler two-fluid model.

CRediT authorship contribution statement

Lauren Schlatter: Writing – original draft, Visualization, Validation, Software, Methodology, Investigation, Formal analysis. **Gabriel**

Gonçalves da Silva Ferreira: Writing – review & editing, Supervision, Software, Methodology, Conceptualization. **Paulo Laranjeira da Cunha Lage:** Writing – review & editing, Supervision, Resources, Methodology, Conceptualization.

Declaration of competing interest

The authors declare the following financial interests/personal relationships which may be considered as potential competing interests: Paulo Laranjeira da Cunha Lage reports financial support was provided by National Council for Scientific and Technological Development. If there are other authors, they declare that they have no known competing financial interests or personal relationships that could have appeared to influence the work reported in this paper.

Appendix A. Grid convergence analysis

See Tables A.15 and A.16.

Table A.15
Estimated uncertainty for the intermediate and finer grids, U_{m2} and U_{m3}, respectively, and global order of accuracy ($\hat{p}_{glb}$) on the determination of the dispersed-phase fraction for all simulated cases. Results are for Solver II for channel flow simulations and Solver V for pipe and Couette flow.

Geometry	U_{m2}	U_{m3}	$\hat{p}_{glb}$
Couette rheometer A – 2D	0.46%	0.21%	1.86
Couette rheometer A – 1D	0.05%	0.03%	1.68
Couette rheometer B	0.13%	0.06%	1.80
Couette rheometer C	0.17%	0.09%	1.87
Eccentric Couette flow	1.99%	0.93%	1.86
Two-dimensional channel A – 2D	0.49%	0.25%	1.73
Two-dimensional channel A – 1D	1.07%	0.73%	1.85
Two-dimensional channel B	0.47%	0.33%	1.72
Two-dimensional channel C	0.24%	0.17%	1.66
Two-dimensional channel D	0.18%	0.12%	1.51
Circular cross-section pipe	0.03%	0.02%	1.89

Table A.16
Estimated uncertainty for the intermediate and finer grids, U_{m2} and U_{m3}, respectively, and global order of accuracy ($\hat{p}_{glb}$) on the determination of the torque on the inner cylinder in all Couette geometries using Solver V.

Geometry	U_{m2}	U_{m3}	$\hat{p}_{glb}$
Couette A	1.60%	0.78%	2.00
Couette B	0.46%	0.22%	2.00
Couette C	0.69%	0.36%	1.85

Appendix B. Anisotropic stress tensor for cylindrical pipe flow

Consider the fully-developed suspension flow at the steady state in a cylindrical pipe of circular cross-section, for which the directions of the velocity, its gradient, and vorticity in cylindrical coordinates are $\hat{\mathbf{e}}_z$, $\hat{\mathbf{e}}_r$, and $\hat{\mathbf{e}}_\theta$, respectively. Hence, the anisotropic stress tensor is

$$\mathbf{Q} = \lambda_1 \hat{\mathbf{e}}_z \hat{\mathbf{e}}_z + \lambda_2 \hat{\mathbf{e}}_r \hat{\mathbf{e}}_r + \lambda_3 \hat{\mathbf{e}}_\theta \hat{\mathbf{e}}_\theta. \tag{B.1}$$

We can derive the corresponding equation in Cartesian coordinates using a simple coordinate system transformation. Expressing the cylindrical unitary vectors in Cartesian coordinates as

$$\hat{\mathbf{e}}_r = \cos\theta \hat{\mathbf{e}}_x + \sin\theta \hat{\mathbf{e}}_y, \qquad \hat{\mathbf{e}}_\theta = \cos\theta \hat{\mathbf{e}}_y - \sin\theta \hat{\mathbf{e}}_x, \tag{B.2}$$

Eq. (B.1) becomes

$$\mathbf{Q} = \lambda_1 \hat{\mathbf{e}}_z \hat{\mathbf{e}}_z + \left(\lambda_2 \cos^2\theta + \lambda_3 \sin^2\theta\right) \hat{\mathbf{e}}_x \hat{\mathbf{e}}_x + \left(\lambda_2 \sin^2\theta + \lambda_3 \cos^2\theta\right) \hat{\mathbf{e}}_y \hat{\mathbf{e}}_y$$
$$+ \left(\lambda_2 - \lambda_3\right) \cos\theta \sin\theta \hat{\mathbf{e}}_y \hat{\mathbf{e}}_x + \left(\lambda_2 - \lambda_3\right) \cos\theta \sin\theta \hat{\mathbf{e}}_x \hat{\mathbf{e}}_y.$$

$$\tag{B.3}$$

Therefore, the components of $\mathbf{Q}$ in Cartesian coordinates are:

(a)	$Q_{xx} = \lambda_2 \cos^2\theta + \lambda_3 \sin^2\theta$	
(b)	$Q_{yy} = \lambda_2 \sin^2\theta + \lambda_3 \cos^2\theta$	
(c)	$Q_{xy} = Q_{yx} = \left(\lambda_2 - \lambda_3\right)\cos\theta$	(B.4)
(d)	$Q_{zz} = \lambda_1$	
(e)	$Q_{xz} = Q_{zx} = Q_{yz} = Q_{zy} = 0$	

The components can be visualised by taking $\theta = \arctan(y/x)$ and plotting each field. However, this formulation features a singularity at $r = 0$, where $\mathbf{Q}$ is undefined.

Appendix C. Supplementary data

Supplementary material related to this article can be found online at https://doi.org/10.1016/j.ijmultiphaseflow.2024.105120.

Data availability

Our improved SBM solver is available at https://github.com/lauschlatter/An-Improved-Suspension-Balance-Model.

References

Badia, A., D'Angelo, Y., Peters, F., Lobry, L., 2022. Frame-invariant modeling for non-Brownian suspension flows. J. Non-Newton. Fluid Mech. 309, 104904. http://dx.doi.org/10.1016/j.jnnfm.2022.104904.

Boggs, P.T., Donaldson, J.R., Byrd, R.H., Schnabel, R.B., 1989. Algorithm 676: ODR-PACK: software for weighted orthogonal distance regression. ACM Trans. Math. Softw. 15 (4), 348–364. http://dx.doi.org/10.1145/76909.76913.

Boyer, F., Guazzelli, E., Pouliquen, O., 2011. Unifying suspension and granular rheology. Phys. Rev. Lett. 107, 188301. http://dx.doi.org/10.1103/PhysRevLett.107.188301.

Coussot, P., Ancey, C., 1999. Rheophysical classification of concentrated suspensions and granular pastes. Phys. Rev. E 59, 4445–4457. http://dx.doi.org/10.1103/PhysRevE.59.4445.

Dbouk, T., Lemaire, E., Lobry, L., Moukalled, F., 2013a. Shear-induced particle migration: Predictions from experimental evaluation of the particle stress tensor. J. Non-Newton. Fluid Mech. 198, 78–95. http://dx.doi.org/10.1016/j.jnnfm.2013.03.006.

Dbouk, T., Lobry, L., Lemaire, E., 2013b. Normal stresses in concentrated non-Brownian suspensions. J. Fluid Mech. 715, 239–272. http://dx.doi.org/10.1017/jfm.2012.516.

Dontsov, E.V., Peirce, A.P., 2014. Slurry flow, gravitational settling and a proppant transport model for hydraulic fractures. J. Fluid Mech. 760, 567–590. http://dx.doi.org/10.1017/jfm.2014.606.

Drijer, I., van de Laar, T., Vollebregt, H.M., Schroën, C.G.P.H., 2018. From highly specialised to generally available modelling of shear induced particle migration for flow segregation based separation technology. Sep. Purif. Technol. 192, 99–109. http://dx.doi.org/10.1016/j.seppur.2017.10.001.

Einstein, A., 1906. Eine neue Bestimmung der Moleküldimensionen. Ann. Der Physik 324, 289–306. http://dx.doi.org/10.1002/andp.19063240204.

Fang, Z., Mammoli, A., Brady, J., Ingber, M., Mondy, L., Graham, A., 2002. Flow-aligned tensor models for suspension flow. Int. J. Multiph. Flow 28, 137–166. http://dx.doi.org/10.1016/S0301-9322(01)00055-6.

Fang, Z., Phan-Thien, N., 1995. Numerical simulation of particle migration in concentrated suspensions by a finite volume method. J. Non-Newton. Fluid Mech. 58 (1), 67–81. http://dx.doi.org/10.1016/0377-0257(94)01355-L.

Fernandes, L.S., 2003. A study of the effect of phase segregation by shear on the rheology of suspensions. (M.Sc. thesis). Programa de Engenharia Química, COPPE/UFRJ.

Gadala-Maria, F., Acrivos, A., 1980. Shear-induced structure in a concentrated suspension of solid spheres. J. Rheol. 24, 799–814. http://dx.doi.org/10.1122/1.549584.

Golub, G.H., van Loan, C.F., 2013. Large sparse linear system problems. In: Matrix Computations. The Johns Hopkins University Press, pp. 597–680.

Greenshields, C., 2019. OpenFOAM v7 User Guide. The OpenFOAM Foundation, London, UK, URL: https://doc.cfd.direct/openfoam/user-guide-v7.

Guazzelli, E., Pouliquen, O., 2018. Rheology of dense granular suspensions. J. Fluid Mech. 852, 748–783. http://dx.doi.org/10.1017/jfm.2018.5489.

Inkson, N., Papoulias, D., Tandon, M., Reddy, V., Lo, S., 2017. An Eulerian-Eulerian formulation of suspension rheology using the finite volume method. J. Non-Newton. Fluid Mech. 245, 38–48. http://dx.doi.org/10.1016/j.jnnfm.2017.05.002.

Jasak, H., 1996. Error analysis and estimation for the finite volume method with applications to fluid flows. (Ph.D. thesis). Imperial College of Science, Technology and Medicine, University of London.

Kang, C., Mirbod, P., 2020. Shear-induced particle migration of semi-dilute and concentrated Brownian suspensions in both Poiseuille and circular Couette flow. Int. J. Multiph. Flow 126, 103239. http://dx.doi.org/10.1016/j.ijmultiphaseflow.2020.103239.

Kang, C., Mirbod, P., 2021. Flow instability and transitions in Taylor–Couette flow of a semidilute non-colloidal suspension. J. Fluid Mech. 916, A12. http://dx.doi.org/10.1017/jfm.2021.75.

Kang, C., Mirbod, P., 2023. Transitions in Taylor-Couette flow of concentrated non-colloidal suspensions. Philos. Trans. Ser. A, Math., Phys., Eng. Sci. 381, 20220126. http://dx.doi.org/10.1098/rsta.2022.0126.

Koh, C.J., Hookham, P., Leal, L.G., 1994. An experimental investigation of concentrated suspension flows in a rectangular channel. J. Fluid Mech. 266, 1–32. http://dx.doi.org/10.1017/S0022112094000911.

Lecampion, B., Garagash, D.I., 2014. Confined flow of suspensions modelled by a frictional rheology. J. Fluid Mech. 759, 197–235. http://dx.doi.org/10.1017/jfm.2014.557.

Leighton, D., Acrivos, A., 1987. The shear-induced migration of particles in concentrated suspensions. J. Fluid Mech. 181, 415–439. http://dx.doi.org/10.1017/S0022112087002155.

Lu, D., Christov, I.C., 2023. Physics-informed neural networks for understanding shear migration of particles in viscous flow. Int. J. Multiph. Flow 165, 104476. http://dx.doi.org/10.1016/j.ijmultiphaseflow.2023.104476.

Lyon, M.K., Leal, L.G., 1998. An experimental study of the motion of concentrated suspensions in two-dimensional channel flow. Part 1. Monodisperse systems. J. Fluid Mech. 363, 25–56. http://dx.doi.org/10.1017/S0022112098008817.

Majji, M.V., Banerjee, S., Morris, J.F., 2018. Inertial flow transitions of a suspension in Taylor–Couette geometry. J. Fluid Mech. 835, 936–969. http://dx.doi.org/10.1017/jfm.2017.754.

Miller, R.M., Morris, J.F., 2006. Normal stress-driven migration and axial development in pressure-driven flow of concentrated suspensions. J. Non-Newton. Fluid Mech. 135, 149–165. http://dx.doi.org/10.1016/j.jnnfm.2005.11.009.

Miller, R.M., Singh, J.P., Morris, J.F., 2009. Suspension flow modeling for general geometries. Chem. Eng. Sci. 64, 4597–4610. http://dx.doi.org/10.1016/j.ces.2009.04.033.

Mills, P., Snabre, P., 1995. Rheology and structure of concentrated suspensions of hard spheres. Shear induced particle migration. J. Phys. II 5, 1597–1608. http://dx.doi.org/10.1051/jp2:1995201.

Mirbod, P., 2016. Two-dimensional computational fluid dynamical investigation of particle migration in rotating eccentric cylinders using suspension balance model. Int. J. Multiph. Flow 80, 79–88. http://dx.doi.org/10.1016/j.ijmultiphaseflow.2015.11.002.

Moraczewski, T., Tang, H., Shapley, N.C., 2005. Flow of a concentrated suspension through an abrupt axisymmetric expansion measured by nuclear magnetic resonance imaging. J. Rheol. 49 (6), 1409–1428. http://dx.doi.org/10.1122/1.2079227.

Morris, J.F., Boulay, F., 1999. Curvilinear flows of noncolloidal suspensions: The role of normal stresses. J. Rheol. 43, 1213–1237. http://dx.doi.org/10.1122/1.551021.

Municchi, F., Nagrani, P.P., Christov, I.C., 2019a. twoFluidsNBSuspensionFoam. https://github.com/fmuni/twoFluidsNBSuspensionFoam/.

Municchi, F., Nagrani, P.P., Christov, I.C., 2019b. A two-fluid model for numerical simulation of shear-dominated suspension flows. Int. J. Multiph. Flow 120, 103079. http://dx.doi.org/10.1016/j.ijmultiphaseflow.2019.07.015.

Nott, P.R., Brady, J.F., 1994. Pressure-driven flow of suspensions: simulation and theory. J. Fluid Mech. 275, 157–199. http://dx.doi.org/10.1017/S0022112094002326.

Oh, S., Song, Y.-q., Garagash, D.I., Lecampion, B., Desroches, J., 2015. Pressure-driven suspension flow near jamming. Phys. Rev. Lett. 114, 088301. http://dx.doi.org/10.1103/PhysRevLett.114.088301.

Passalacqua, A., Fox, R., 2011. Implementation of an iterative solution procedure for multi-fluid gas–particle flow models on unstructured grids. Powder Technol. 213, 174–187. http://dx.doi.org/10.1016/j.powtec.2011.07.030.

Patankar, S.V., Spalding, D.B., 1972. A calculation procedure for heat, mass and momentum transfer in three-dimensional parabolic flows. Int. J. Heat Mass Transfer 15, 1787–1806. http://dx.doi.org/10.1016/0017-9310(72)90054-3.

Phan-Thien, N., Graham, A.L., Altobelli, S.A., Abbott, J.R., Mondy, L.A., 1995. Hydrodynamic particle migration in a concentrated suspension undergoing flow between rotating eccentric cylinders. Ind. Eng. Chem. Res. 34 (10), 3187–3194. http://dx.doi.org/10.1021/ie00037a002.

Phillips, R.J., Armstrong, R.C., Brown, R.A., Graham, A.L., Abbott, J.R., 1992. A constitutive equation for concentrated suspensions that accounts for shear induced particle migration. Phys. Fluids A 4, 30–40. http://dx.doi.org/10.1063/1.858498.

Ramesh, P., Alam, M., 2020. Interpenetrating spiral vortices and other coexisting states in suspension Taylor-Couette flow. Phys. Rev. Fluids 5, 042301(R). http://dx.doi.org/10.1103/PhysRevFluids.5.042301.

Ramesh, P., Bharadwaj, S., Alam, M., 2019. Suspension Taylor–Couette flow: co-existence of stationary and travelling waves, and the characteristics of Taylor vortices and spirals. J. Fluid Mech. 870, 901–940. http://dx.doi.org/10.1017/jfm.2019.291.

Rhie, C.M., Chow, W.L., 1983. Numerical study of the turbulent flow past an airfoil with trailing edge separation. AIAA J. 21, 1525–1532. http://dx.doi.org/10.2514/3.8284.

Schroën, K., van Dinther, A., Stockmann, R., 2017. Particle migration in laminar shear fields: A new basis for large scale separation technology? Sep. Purif. Technol. 174, 372–388. http://dx.doi.org/10.1016/j.seppur.2016.10.057.

Siqueira, I.R., de Souza Mendes, P.R., 2019. On the pressure-driven flow of suspensions: Particle migration in apparent yield-stress fluids. J. Non-Newton. Fluid Mech. 265, 92–98. http://dx.doi.org/10.1016/j.jnnfm.2019.02.002.

Subia, S., Ingber, M., Mondy, L., Altobelli, S., Graham, A., 1998. Modeling of concentrated solutions using a continuum constitutive equation. J. Fluid Mech. 373, 193–219. http://dx.doi.org/10.1017/S0022112098002651.

Tiwari, P., Antal, S.P., Podowski, M.Z., 2009. Modeling shear-induced diffusion force in particulate flows. Comput. & Fluids 38, 727–737. http://dx.doi.org/10.1016/j.compfluid.2008.09.007.

Weller, H.G., Tabor, G., Jasak, H., Fureby, C., 1998. A tensorial approach to computational continuum mechanics using object-oriented techniques. Comput. Phys. 12, 620–631. http://dx.doi.org/10.1063/1.168744.

Yadav, S., Mallela, M.R., Singh, A., 2015. Shear induced migration of concentrated suspension through Y-shaped bifurcation channels. Particul. Sci. Technol. 34, 83–95. http://dx.doi.org/10.1080/02726351.2015.1051684.